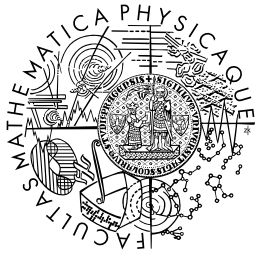

FACULTY
OF MATHEMATICS
AND PHYSICS
Charles University

MASTER THESIS

Michal Lelák

Study of the double-Dalitz decay of neutral pion at the NA62 experiment

Institute of Particle and Nuclear Physics

Supervisor of the master thesis: Mgr. Michal Koval', Ph. D.
Study programme: Particle and Nuclear Physics
Study branch: FCJFP

Prague 2024

I declare that I carried out this master thesis independently, and only with the cited sources, literature and other professional sources. It has not been used to obtain another or the same degree.

I understand that my work relates to the rights and obligations under the Act No. 121/2000 Sb., the Copyright Act, as amended, in particular the fact that the Charles University has the right to conclude a license agreement on the use of this work as a school work pursuant to Section 60 subsection 1 of the Copyright Act.

In ..... date ....

Author's signature

I would like to express my sincere gratitude to my supervisor, Michal Kovaľ, for his continuous support, guidance, and friendly attitude. His vast knowledge and invaluable advice were instrumental in shaping this thesis. I also want to thank my family and girlfriend Gabriela for their love and support.

Title: Study of the double-Dalitz decay of neutral pion at the NA62 experiment

Author: Michal Lelák

Institue: Institute of Particle and Nuclear Physics

Supervisor: Mgr. Michal Kovaľ, Ph. D., Institute of Particle and Nuclear Physics

Abstract: The NA62 experiment at CERN represents leading physics research of rare kaon decays. The NA62 aims to measure the $K^+ \to \pi^+\nu\overline{\nu}$ decay branching ratio which is approximately 10^{-10}. Any significant discrepancy between the measured value and the Standard Model (SM) prediction would hint at physics beyond the SM. Other rare kaon and pion decays can also be studied at NA62. The measurements of neutral pion decays, such as the double Dalitz decay $\pi^0 \to e^+e^-e^+e^-$, provide important input to the theoretical modeling of form factor describing the π^0 decays and interactions. In 2017 – 2018, the NA62 experiment collected a large data sample (Run 1) of the K^+ decays with electron-positron pairs in the final state. In our analysis of the data sample, 1143 π^0 double Dalitz decays were identified. The measured branching ratio of the decay is inclusive of final state photon radiation and reads $B(\pi^0 \to e^+e^-e^+e^-(\gamma), x_{4e} > 0.9) = (3.12 \pm 0.17) \times 10^{-5}$. The result is compatible with previous measurements. The important part of the analysis is the study of five-track reconstruction efficiency in Run 1 data and simulated samples of five-track decays.

Keywords: neutral pion, rare decays, NA62, CERN

Názov: Štúdium dvojitého Dalitzovho rozpadu neutrálneho piónu v experimente NA62

Autor: Michal Lelák

Ústav: Ústav časticovej a jadrovej fyziky

Vedúci: Mgr. Michal Kovaľ, Ph. D., Ústav časticovej a jadrovej fyziky

Abstrakt: Experiment NA62 v CERN-e je svetovým lídrom vo výskume vzácnych rozpadov kaónov. Hlavným cieľom experimentu je zmerať vetviaci pomer rozpadu $K^+ \to \pi^+\nu\overline{\nu}$, ktorý je približne 10^{-10}. Akákoľvek výraznejšia odchýlka medzi nameranou hodnotou a hodnotou určenou Štandardným modelom by znamenala objav fyziky za hranicami Štandardného modelu. Predmetom výskumu sú však aj iné vzácne rozpadové módy kaónov a piónov. Štúdium vzácnych rozpadov neutrálneho piónu, ako je dvojitý Dalitzov rozpad $\pi^0 \to e^+e^-e^+e^-$, poskytuje dôležitý vstup pre teoretické modelovanie formfaktora, ktorý popisuje rozpady a interakcie neutrálnych piónov. Experiment NA62 zhromaždil v rokoch 2017 – 2018 veľký súbor dát (Run 1) rozpadov nabitého kaónu s elektrón-pozitrónovými pármi v koncovom stave. Našou analýzou bolo v dátach identifikovaných 1143 dvojitých Dalitzových rozpadov neutrálneho piónu. Hodnota vetviaceho pomeru tohto rozpadu zahrňujúca prípady s možným vyžiareným fotónom v koncovom stave je $B(\pi^0 \to e^+e^-e^+e^-(\gamma), x_{4e} > 0.9) = (3.12 \pm 0.17) \times 10^{-5}$. Tento výsledok je kompatibilný s predchádzajúcimi meraniami. Dôležitou súčasťou analýzy je aj štúdium efektivity rekonštrukcie dráh nabitých častíc v Run 1 dátach a simulovaných dátach päťčasticových rozpadov.

Kľúčové slová: neutrálny pión, vzácne rozpady, NA62, CERN

Contents

Introduction

The Standard Model (SM) of particle physics is a theoretical framework that describes the fundamental particles and their interactions, excluding gravity [1, 2, 3, 4]. It has successfully explained a wide range of phenomena observed in particle physics experiments. Despite its success, the Standard Model has limitations, such as its inability to incorporate gravity or account for phenomena like dark matter, neutrino masses, and neutrino oscillation. These observed phenomena need to be explained by new physics beyond the SM.

Charged and neutral kaons ($K^{\pm}$, K^0, $\bar{K}^0$) belong to the group of strange mesons [5]. Experiments investigating kaons played a pivotal role in the development of the SM of particle physics. Notably, in 1964, the observation of CP symmetry violation in neutral kaon decays marked a significant milestone [6]. This groundbreaking discovery spurred further research in kaon physics, leading to experiments such as KTeV at Fermilab [7] and the NA48 experiment at CERN [8].

The NA62 (North Area 62) experiment at CERN is dedicated to measuring the rate of the exceptionally rare kaon decay $K^+ \to \pi^+ \nu\overline{\nu}$ [9]. The primary objective is to determine this branching ratio with a precision of 10% and compare it with the Standard Model prediction. Any significant deviation between experimental and theoretical results could hint at physics beyond the Standard Model.

Pion decays can also be studied at NA62 in addition to charged kaon decays. One of such decays is the rare double Dalitz decay $\pi^0 \to e^- e^+ e^- e^+$ with branching ratio $B(\pi^0 \to e^- e^+ e^- e^+) = (3.34 \pm 0.16) \times 10^{-5}$ [5] measured previously at the experiment KTeV-E799 at Fermilab. The main goal of this thesis is to measure the branching ratio of this decay with relative precision comparable to the precision of KTeV results (around 5 %).

The physics background is described in chapter 1. The chapter 2 outlines the NA62 setup, and the relevant detectors are described in more detail. The chapter 3 contains a detailed procedure for the analysis, including the results.

1. Physics Background

1.1 Kaon physics

The kaon discovery dates back to 1947 when it was first observed in a cloud chamber experiment studying cosmic ray events [10]. Initially, the nature of this particle remained unknown, although two distinct versions were identified: a neutral variant decaying into two charged pions and a charged version decaying into a charged pion and a neutral particle. Two years later, a similar particle was observed decaying into three pions, prompting what became known as the $\theta - \tau$ problem. This dilemma arose from the observation that the same particle was decaying into two different final states with different parities [11], ultimately leading to the realization that weak interactions do not conserve parity.

Further observations and measurements in the early 1950s gradually elucidated the properties of this enigmatic particle, eventually leading to its designation as the K-meson, comprising four types: K^+, K^-, K^0 and $\bar{K}^0$. These studies revealed that while the kaon lifetimes were notably lengthy, their production occurred at a much faster rate. This phenomenon prompted the introduction of a new quantum number, strangeness, as a hypothesis [12, 13]. The concept of strangeness conservation in strong interactions, yet its violation in weak interactions, emerged as a fundamental aspect of understanding the behavior of kaons. The neutral kaons K^0 and $\bar{K}^0$ are not physical states. The neutral kaon decay studies showed that two combinations of K^0 and $\bar{K}^0$ correspond to the physical states – K^0_L with lifetime $c\tau \approx 15$ m and K^0_S with lifetime $c\tau \approx 3$ cm. The basic properties of kaons are summarized in table 1.1 and the most abundant decays of charged kaons in table 1.2.

Table 1.1: Kaon quark content and masses [5].

Particle	Quark content	Mass [MeV/c^2]
K^+	$u\bar{s}$	493.677 ± 0.016
K^-	$\bar{u}s$	493.677 ± 0.016
K^0	$d\bar{s}$	497.611 ± 0.013
$\bar{K}^0$	$\bar{d}s$	497.611 ± 0.013

Table 1.2: The most abundant K^+ decay modes and their branching fractions [5].

Decay mode	Branching ratio
$K^+ \to \mu^+\nu_\mu$	$(63.56 \pm 0.11)\%$
$K^+ \to \pi^+\pi^0$	$(20.67 \pm 0.08)\%$
$K^+ \to \pi^+\pi^+\pi^-$	$(5.583 \pm 0.024)\%$
$K^+ \to \pi^0 e^+\nu_e$	$(5.07 \pm 0.04)\%$
$K^+ \to \pi^0\mu^+\nu_\mu$	$(3.352 \pm 0.033)\%$
$K^+ \to \pi^+\pi^0\pi^0$	$(1.760 \pm 0.023)\%$

1.2 $K^+ \to \pi^+ \nu\overline{\nu}$ Decay

Among the numerous flavor-changing neutral current (FCNC) decays observed in K and B mesons, the exceedingly rare decays $K \to \pi\nu\overline{\nu}$ play a pivotal role in the quest for BSM physics search. These decays are characterized by their theoretical cleanliness and strong suppression, with their branching ratios calculated to high precision within the framework of the SM. Therefore, even minor deviations from the SM predictions detected in experiments would potentially signify new physics.

The $K^+ \to \pi^+ \nu\overline{\nu}$ decay is based on $\overline{s} \to \overline{d}\nu\overline{\nu}$ transition. The main contributions within SM come from electroweak penguin (Z boson exchange) and box (W boson exchange) diagrams, which are depicted on fig. 1.1 [14]. Detailed computations of the decay branching ratio $B_{SM}(K^+ \to \pi^+\nu\overline{\nu}) = (9.11 \pm 0.72) \times 10^{-11}$ [15] can be found in [16].

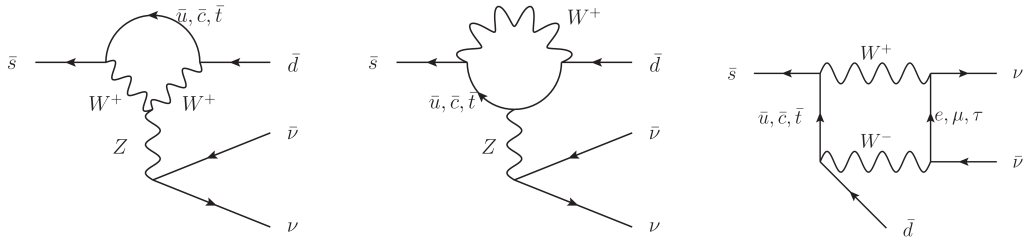

Figure 1.1: Feynmann diagrams of $K^+ \to \pi^+\nu\overline{\nu}$. Figure from [14].

Previously, the $K^+ \to \pi^+\nu\overline{\nu}$ branching ratio was measured by the E949 experiment at Brookhaven National Laboratory, yielding

$$B_{E949}(K^+ \to \pi^+\nu\overline{\nu}) = (1.73^{+1.15}_{-1.05}) \times \ 10^{-10} [17]. \tag{1.1}$$

However, this result was based on the observation of only seven events. Therefore, NA62 aims to obtain a more extensive sample size of about 100 events.

Recent findings from NA62 report a branching fraction measurement of

$$B_{NA62}(K^+ \to \pi^+\nu\overline{\nu}) = (10.6^{+4.0}_{-3.4}|_{\text{stat}} \pm 0.9|_{\text{syst}}) \times 10^{-11}, \tag{1.2}$$

derived from the observation of 20 signal candidates with an expected background of 7 events from the overall data sample collected during 2016–2018 [18]. A new data collection run commenced in 2021, intending to gather additional data to get closer to the original goal of the NA62 experiment.

1.3 The π^0 Double Dalitz Decay

In 1934, Hideki Yukawa suggested that the carrier particles of the strong nuclear forces were mesons with a mass of approximately 100 MeV/c^2 [19], nowadays known as pions (charged $\pi^\pm$ and neutral π^0). The main decay mode of the neutral pion was suggested to be the decay into two photons with the lifetime $\sim 10^{-16}$ s [20].

The charged pion was observed in 1947 in cosmic rays by Cecil Powell *et al.* at the University of Bristol. They observed pion captures by protons and pion decays into muons in a photographic emulsion [21].

Since the neutral pion does not directly leave a track in a photographic emulsion, it is more difficult to detect it, and the tracks of the decay products have to be used. The first π^0 decay into two photons was observed at the University of California's cyclotron in 1950 [22]. Photons with energies up to 200 MeV created by the proton collisions with various targets were detected. The observed spectral and angular distributions aligned with those expected from a neutral meson. This meson, characterized by a mass approximately 300 times that of the electron and a lifetime shorter than 10^{-11} s, underwent decay into two photons.

The neutral pion, being the lightest meson, is significant in investigating the low-energy characteristics of the strong nuclear force. Below is a summary table detailing its fundamental properties.

Table 1.3: π^0 physical properties [5].

Particle symbol	π^0
Quark content	$(u\bar{u} - d\bar{d})/\sqrt{2}$
Quantum numbers	$I^G(J^{PC}) = 1^{-1}(0^{-+})$
Mass	(134.9766 ± 0.0006) MeV/c^2
Mean lifetime	$(8.52 \pm 0.18) \times 10^{-17}$ s

In 99% of cases, the π^0 decays into two photons (fig. 1.2a), but other decay modes also occur, such as the Dalitz decay $\pi^0 \to \gamma e^+ e^-$ (fig. 1.2b), the double Dalitz decay $\pi^0 \to e^+ e^- e^+ e^-$ (fig. 1.2c) and the $\pi^0 \to e^+ e^-$ decay (fig. 1.2d). The branching ratios of individual modes are listed in table 1.4.

Table 1.4: The branching ratios of π^0 decays [5].

Decay	Branching ratio
$\pi^0 \to \gamma\gamma$	$(98.823 \pm 0.034)\%$
$\pi^0 \to e^+ e^- \gamma$	$(1.174 \pm 0.035)\%$
$\pi^0 \to e^+ e^- e^+ e^-$	$(3.34 \pm 0.16) \times 10^{-5}$
$\pi^0 \to e^+ e^-$	$(6.46 \pm 0.33) \times 10^{-8}$

The shaded blobs in the fig. 1.2 stand for the transition form factor F, which is a function of the normalized momentum transfer x_i of the off-shell photons defined via the invariant masses of the individual electron-positron pairs

$$x_i = \left(\frac{m^i_{e^+e^-}}{m_{\pi^0}} \right)^2 = \frac{(p^i_{e^+} + p^i_{e^-})^2}{m^2_{\pi^0}}. \tag{1.3}$$

In the case of the Dalitz decay, only one off-shell photon is present, so $F(x_1, x_2) = F(x, 0) = F(x)$ and in the decay into two photons, the form factor becomes a constant $F(x_1, x_2) = F(0, 0) = F$.

A particle form factor encodes the information about its internal structure and the interactions with other particles without including the underlying physics. For instance, the π^0 transition form factor (TFF) characterizes the electromagnetic properties of the neutral pion, and, within the Standard Model (SM), it arises from quantum chromodynamics. A typical feature of electromagnetic interactions among hadrons involves the separation of a differential decay width ($d\Gamma$) or a cross-section ($d\sigma$) into two components: one attributed to the point-like (p-l)

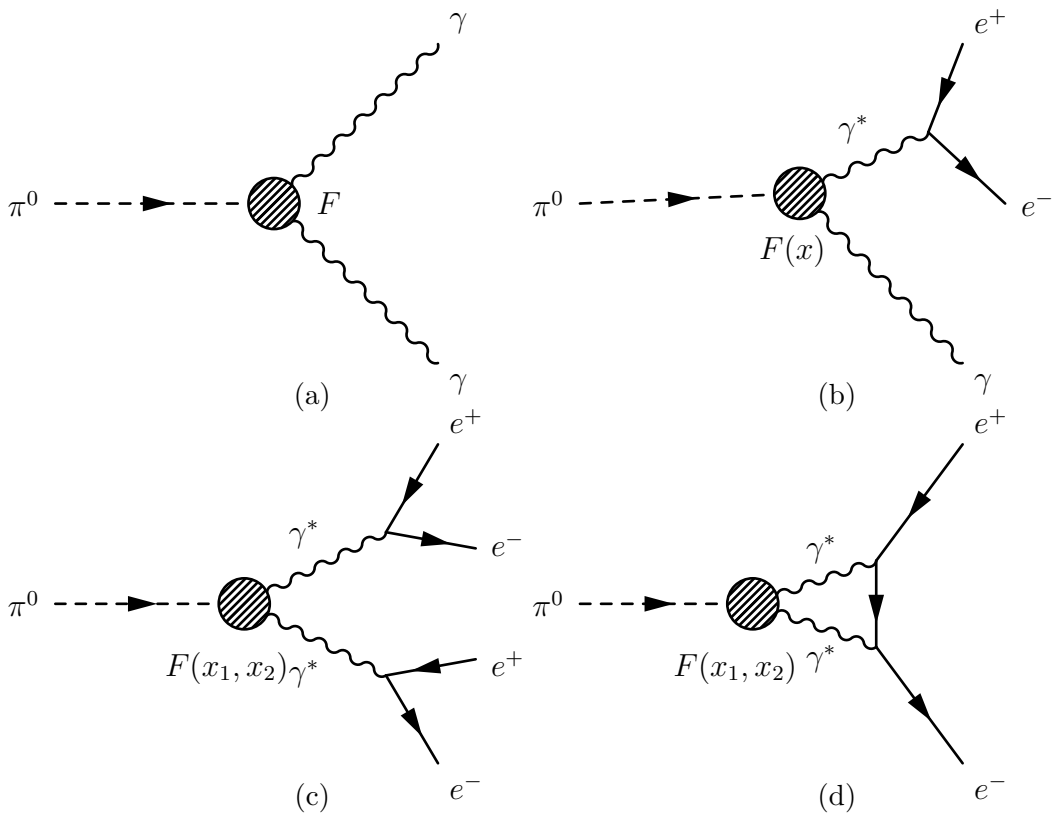

Figure 1.2: Feynamn diagrams of the π^0 decays. The shaded blobs in the diagrams refer to the so-called form factor discussed in this section.

interaction between the particles involved and the other arising from the form factor F

$$\begin{aligned} \frac{d\sigma}{dx_1 dx_2} &= \left.\frac{d\sigma}{dx_1 dx_2}\right|_{\text{p-l}} |F(x_1, x_2)|^2, \\ \frac{d\Gamma}{dx_1 dx_2} &= \left.\frac{d\Gamma}{dx_1 dx_2}\right|_{\text{p-l}} |F(x_1, x_2)|^2. \end{aligned} \tag{1.4}$$

Since the thesis is not focused on the TFF measurement, a more detailed form factor description can be found in [14, 23, 24].

1.3.1 Radiative Corrections

This section's description of higher-order double Dalitz processes summarizes the detailed publication on radiative corrections, their effect on the invariant mass distributions, and angular correlations in [25].

The tree-level double Dalitz process depicted in fig. 1.2c is $O(\alpha^2)$ since the diagram contains two electromagnetic vertices. However, higher-order processes where one or more internal loops occur also affect the final branching ratio and must be considered. Three types of graphs contribute at $O(\alpha^4)$: the vacuum polarization (fig. 1.3a), the vertex correction (fig. 1.3b), and the 5-point diagram (fig. 1.3c). The interference terms between the tree-level and one-loop diagrams are $O(\alpha^3)$ and contribute to the first-order radiative correction to the double Dalitz rate.

The vertex correction and the 5-point graph contain IR divergences (in the zero limit of the exchanged photon energy). However, the radiative double Dalitz decay $\pi^0 \to e^+e^-e^+e^-\gamma$ contributions (fig. 1.4) cancel the mentioned singularities and the decay rate becomes finite.

From the experimental point of view, the radiative corrections play a key role in determining the double Dalitz branching ratio. Extra photons in the final state carry away some part of the invariant mass, which is typically used to identify the decay in a measurement. The distinction between non-radiative and radiative decay is typically made by a cut on the photon energy in the pion rest frame or by the invariant variable x_{4e}

$$x_{4e} = \frac{m^2_{eeee}}{m^2_{\pi^0}}, \tag{1.5}$$

where m_{eeee} is the invariant mass of the four electrons in the final state. The radiation probability is defined as a fraction $P = \Gamma_{4e\gamma}/\Gamma_{4e(\gamma)}$, where $\Gamma_{4e\gamma}$ is the decay width of the radiative process (with a maximum cut-off on x_{4e}) and $\Gamma_{4e(\gamma)}$ represents the decay width of the combined process, including one-photon radiation. The probability values mentioned in [25] are $P(x_{4e} < 0.9985) = 0.187$, $P(x_{4e} < 0.95) = 0.058$. The radiative corrections were also studied in the NA62 experiment by Tomáš Husek who evaluated $P(x_{4e} < 0.9985) = 0.189$, $P(x_{4e} < 0.95) = 0.054$, and $P(x_{4e} < 0.90) = 0.032$ [26]. These values correspond to the inclusive radiative double Dalitz decay generator implemented and used in the presented analysis.

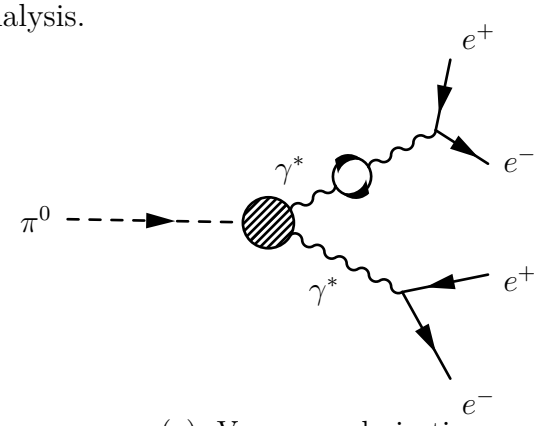

(a) Vacuum polarization.

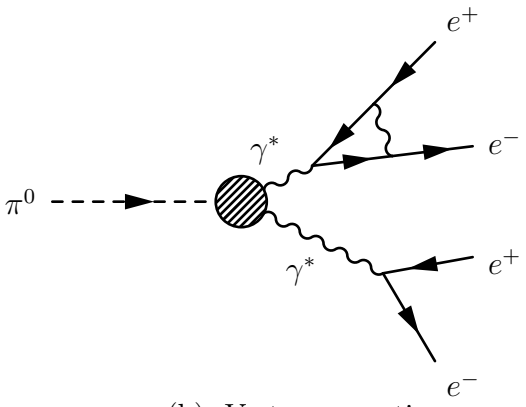

(b) Vertex correction.

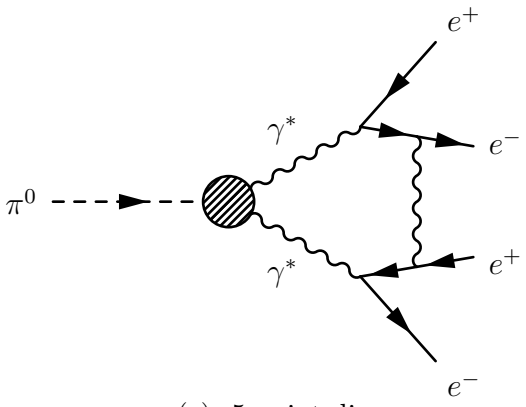

(c) 5-point diagram.

Figure 1.3: Higher-order double Dalitz diagrams – virtual corrections. The final state consists of two electron-positron pairs.

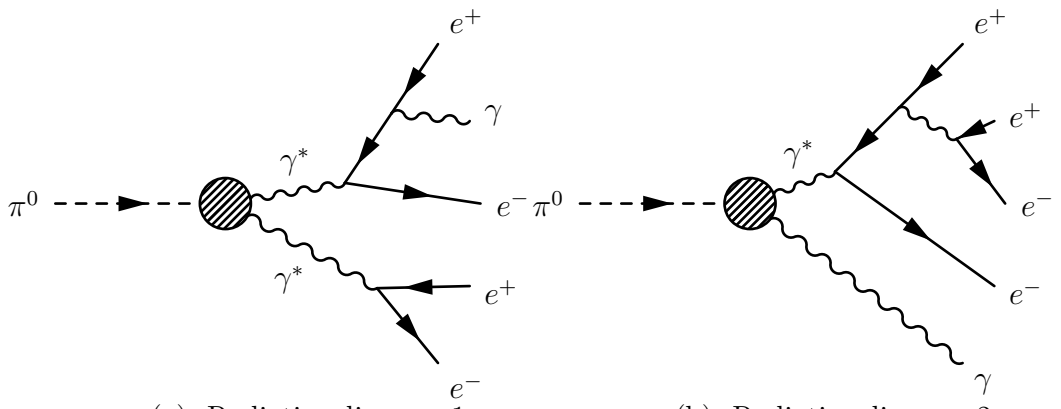

(a) Radiative diagram 1. (b) Radiative diagram 2.

Figure 1.4: Higher-order double Dalitz diagrams – radiative decays. The final state consists of two electron-positron pairs and an extra photon.

1.4 Experimental Status

The most precise experimental information on the π^0 double Dalitz branching ratio comes from the KTeV-E799 experiment at Fermilab. This section summarizes the measurement described in [27].

The analysis at KTeV is based on the reconstruction of the decay $K_L \to \pi^0\pi^0\pi^0$. The essential KTeV detectors for the analysis are a drift chamber-based charge particle spectrometer and a cesium iodide (CsI) electromagnetic calorimeter. The chamber-based spectrometer serves for the charged track reconstruction and the CsI for the particle energy measurement.

The π^0 double Dalitz decay branching ratio measurement is based on the signal mode identification and the normalization mode identification. The signal mode is the decay $K_L \to \pi^0\pi^0\pi^0_{DD}$ where the π^0_{DD} stands for the double Dalitz decay $\pi^0 \to e^+e^-e^+e^-$. The signature of this mode is four charged particles identified as electrons with their invariant mass corresponding to the mass of π^0 and two pairs of photons compatible with the remaining two π^0's. The invariant mass of these eight final particles has to be consistent with the K_L mass.

The normalization mode used in the analysis is $K_L \to \pi^0\pi^0_D\pi^0_D$ where the π^0_D is a short notation for the Dalitz decay $\pi^0 \to e^+e^-\gamma$. The great advantage of such a choice is the similarity of the modes because the final state particles are identical. This leads to the cancellation of most detector-related systematic effects in the branching ratio measurement.

The most significant background to both modes is the process $K_L \to \pi^0\pi^0\pi^0_D$ and the subsequent external conversion of a photon coming from the $\pi^0 \to \gamma\gamma$ decay or the single Dalitz decay. Another background is the decay $K_L \to \pi^0\pi^0\pi^0 \to 6\gamma$, where two photons convert.

The backgrounds are successfully suppressed by requiring a track separation at the first drift chamber greater than 2 mm, which removed 99.74% of the remaining simulated background while preserving 74.3% of signal and 72.7% of normalization events.

The only remaining task is to distinguish between the signal and the normalization mode. This is realized by a χ^2 formed of the three reconstructed π^0 masses. The event with the smaller χ^2 is tagged as the signal. This method correctly identifies 99.5% of events.

The final sample consists of 30 511 signal events with 0.6% residual background and 141 251 normalization events with a 0.5% background. The main source of the background is the misidentification of signal and normalization events.

Except for the experimental data, the Monte Carlo simulation must also be used to estimate acceptancies, which enter the branching ratio measurement. The following formula expresses the fraction of the signal branching ratio (B_{eeee}) multiplied by the branching ratio of $\pi^0 \to \gamma\gamma$ ($B_{\gamma\gamma}$) divided by the square of the Dalitz decay branching ratio ($B_{ee\gamma}$):

$$\begin{aligned}\frac{B_{eeee} \cdot B_{\gamma\gamma}}{B_{ee\gamma}^2} =& \frac{N(K_L \to \pi^0\pi^0\pi^0_{DD})}{N(K_L \to \pi^0\pi^0_D\pi^0_D)} \\ & \cdot \frac{\epsilon(K_L \to \pi^0\pi^0_D\pi^0_D)}{\epsilon(K_L \to \pi^0\pi^0\pi^0_{DD})},\end{aligned} \tag{1.6}$$

where N is the number of selected events and ϵ is the combined geometric acceptance and detection efficiency for a given mode.

Radiative corrections bring certain complications to the measurement. The variable x_{4e} (eq. (1.5)) defines the kinematic region for which the inclusive branching ratio is measured: $x_{4e} > 0.9$. The final result is

$$\frac{B_{eeee}^{x>0.9} \cdot B_{\gamma\gamma}}{B_{ee\gamma}^2} = 0.2245 \pm 0.0014_{\text{stat}} \pm 0.0009_{\text{syst}}. \tag{1.7}$$

Using the known values $B_{\gamma\gamma} = 0.9880 \pm 0.0003$ and $B_{ee\gamma} = (1.198 \pm 0.032) \times 10^{-2}$, the signal branching ratio is

$$B_{eeee}^{x>0.9} = (3.26 \pm 0.18) \times 10^{-5}, \tag{1.8}$$

where the error is dominated by the external uncertainty of $B_{ee\gamma}$. Extension to all radiative states using the model described in [25] yields

$$\frac{B_{eeee(\gamma)} \cdot B_{\gamma\gamma}}{B_{ee\gamma\gamma}^2} = 0.2383 \pm 0.0015_{\text{stat}} \pm 0.0010_{\text{syst}}, \tag{1.9}$$

$$B_{eeee(\gamma)} = (3.46 \pm 0.19) \times 10^{-5}. \tag{1.10}$$

2. The NA62 Experiment

2.1 Experimental Overview

The NA62 experiment at the SPS accelerator at CERN is dedicated to the research of very rare kaon and pion decays. The main goal is the $K^+ \to \pi^+\nu\overline{\nu}$ branching ratio measurement with 10% precision and its comparison with the SM prediction. Since this branching ratio is approximately 10^{-10}, for the detection of 100 such events accounting for 10% detection acceptance, 10^{13} kaon decays must occur in the fiducial region. Additionally, a suppression factor of 10^{11} for background processes, such as other kaon decays (table 1.2), is needed to get a signal-to-background ratio that allows a precise measurement of the branching ratio.

The signal decay is identified by observing precisely one kaon and one pion track. Background suppression is primarily achieved through kinematic rejection, utilizing the variable m^2_{miss}, defined as

$$m^2_{\text{miss}} = (P_K - P_\pi)^2, \tag{2.1}$$

where P_K and P_π represent the four-momenta of the incoming kaon and the outgoing pion, respectively. The m^2_{miss} distribution for the most common kaon decay modes is shown in fig. 2.1.

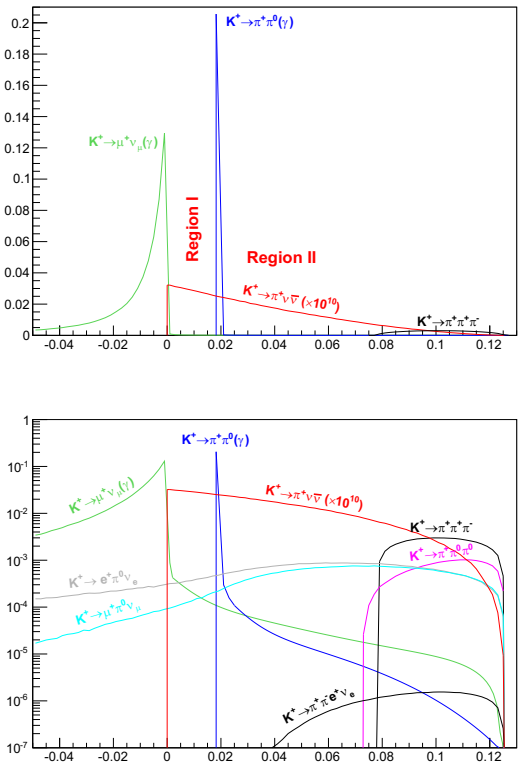

Figure 2.1: The m^2_{miss} distribution for various kaon decays in linear (top) and logarithmic (bottom) scales. $K^+ \to \pi^+\nu\overline{\nu}$ signal is multiplied by 10^{10}. Figure from [9].

By defining the signal regions for the $K^+ \to \pi^+\nu\bar{\nu}$ decay (Region I and Region II in fig. 2.1), a rejection factor of 10^5 for common kaon decays can be achieved. To accurately identify the sharp peak between these regions, corresponding to the $K^+ \to \pi^+\pi^0$ decay (fig. 2.1), it is essential to measure m^2_{miss} with high precision.

2.2 NA62 Beam and Detector

2.2.1 Experimental layout

A 400 GeV/c proton beam, generated by the CERN SPS accelerator, interacts with a target to produce a 75 GeV/c hadron beam traveling along the z axis of the experimental coordinate system. The resultant momentum of the kaon decay products typically falls within the range of 10 – 50 GeV/c, with their transverse momentum constrained by the K^+ mass of 493.7 MeV/c^2.

Kaons in the beam are identified using the CEDAR differential Cherenkov counter equipped with the KTAG photon detection system. The kaon tracks are subsequently reconstructed using the beam spectrometer GTK. Charged particles originating from the kaon decay are then reconstructed by the Straw spectrometer.

Decays with a muon in the final state, such as the most frequent decay $K^+ \to \mu^+\nu_\mu$, can be suppressed through particle identification. Pion/muon separation is achieved using the Ring Imaging Cherenkov detector (RICH) located downstream of the Straw spectrometer, as well as the calorimeters LKr, MUV1, MUV2, and a plane of scintillating tiles MUV3 (fig. 2.2).

Events involving neutral pions and photons in the final state, such as the decay $K^+ \to \pi^+\pi^0$, are suppressed through photon rejection. The π^0 decays almost immediately into two photons, with a lifetime of approximately 0.9×10^{-17} s [5]. These photons are detected by the electromagnetic calorimeters LAV, LKr, IRC, and SAC. The NA62 experimental setup is depicted in fig. 2.2.

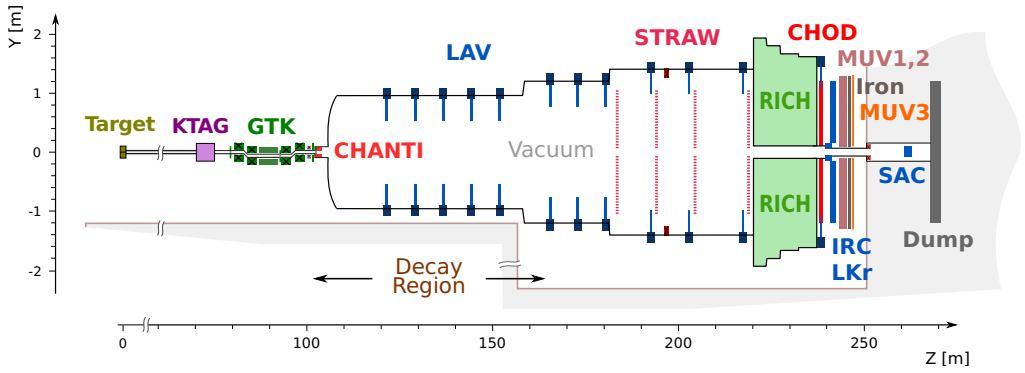

Figure 2.2: The NA62 experimental layout. Figure from [9].

The following text describes the NA62 beam and the detectors used in the presented analysis.

2.2.2 K12 Beam Line

The primary beam comprises 400 GeV/c protons produced at the SPS accelerator and directed via the P42 beam line to the T10 target (400 mm long, 2 mm diameter beryllium). The secondary hadron beam (K12) is derived at a central momentum of +75 GeV/c to maximize the kaon production rate. The K12 beam line layout is designed to maximize the acceptance using the focusing quadrupole magnets (Q1 - Q10) and to minimize the background composed of the primary beam particles and unwanted secondary beam particles using achromats (A1 and A2), collimators (C1 - C7), and beam-dump units (TAX1 and TAX2). This is schematically illustrated by fig. 2.3. More details about the function of individual layout elements can be found in [9].

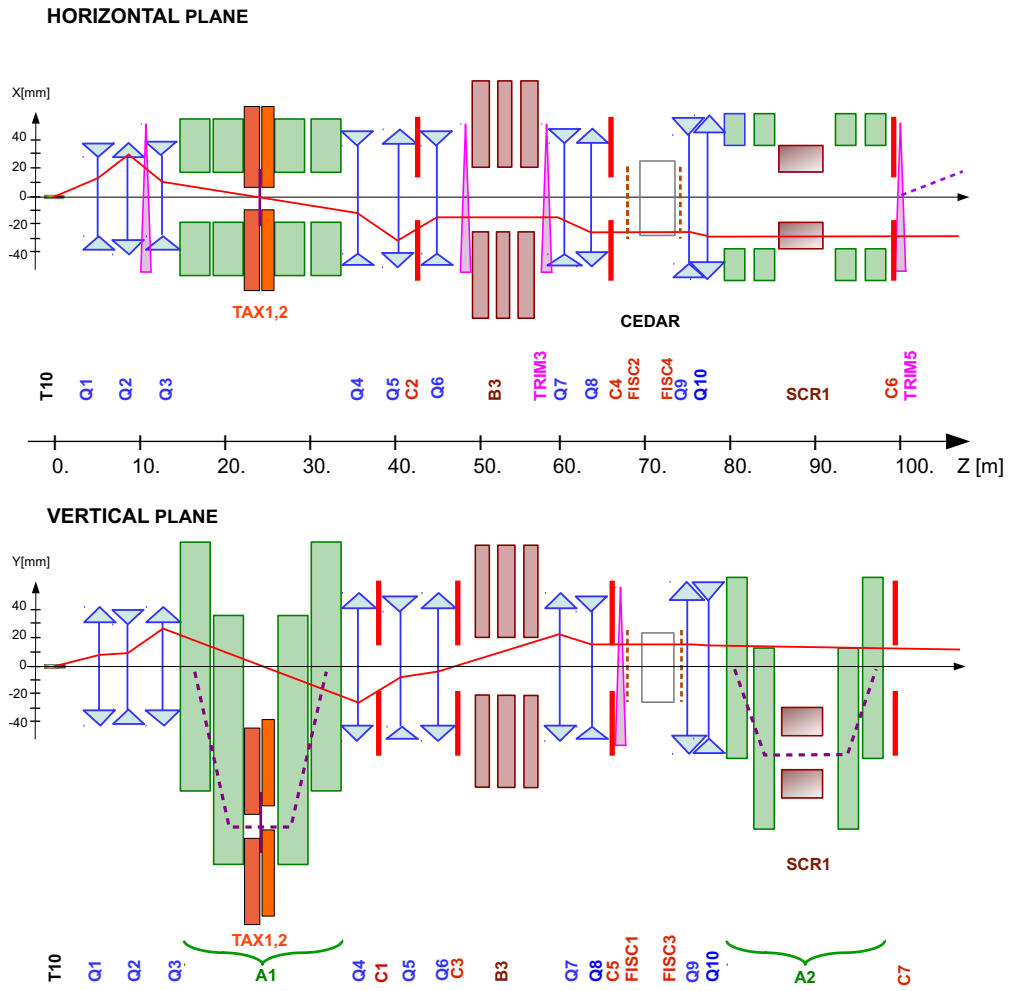

Figure 2.3: The K12 beam line layout from the target T10 to the entrance of the decay region. Figure from [9].

A horizontal steering magnet (TRIM5) deflects the beam in the x direction by an angle of +1.2 mrad, which is then deflected by -3.6 mrad in the x direction by the downstream spectrometer magnet MNP33. The beam finally passes through the central aperture of the LKr calorimeter (fig. 2.4). The principal properties of the high-intensity K^+ beam are summarized in table 2.1.

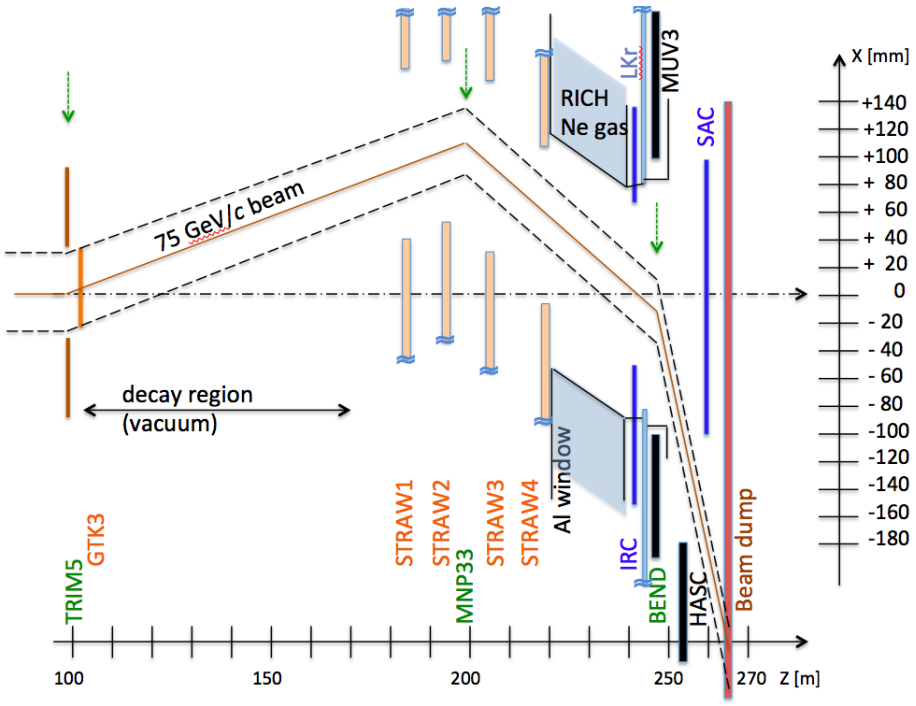

Figure 2.4: The K12 beam line layout through the decay region and the detectors in the (X, Z) plane. Figure from [9].

Table 2.1: The principal characteristics of the high-intensity K^+ beam [9].

Beam acceptance	Horizontal	$\pm$ 2.7 mrad
	Vertical	$\pm$ 1.5 mrad
K^+ momentum	mean momentum	75 GeV/c
	Effective $\Delta p/p$	1.6%
	$\Delta p/p$ rms	1.0%
Divergence at CEDAR (rms)	Horizontal	0.07 mrad
	Vertical	0.07 mrad
Divergence at GTK (rms)	Horizontal	0.11 mrad
	Vertical	0.11 mrad
Beam size at GTK (rms)	Horizontal	$\pm$ 26.4 mm
	Vertical	$\pm$ 12.0 mm
Fiducial decay length:		60 m
ΔZ = fiducial decay length/decay length		0.107
Decay fraction:	$(1 - e^{-\Delta z})$	0.101
Instantaneous beam rates	p	173 MHz (23%)
	K^+	45 MHz (6%)
	π^+	525 MHz (70%)
	μ^+	$\sim$ 5 MHz ($<$ 1%)
	Total	750 MHz (100%)
Total beam flux per pulse		2.25×10^9
Estimated K^+ decays per year		5×10^{12}

2.2.3 Kaon Tagger (KTAG)

As shown in table 2.1, kaons form just 6% of the K12 beam and are identified by the KTAG detector. The differential Cherenkov counter CEDAR with the

gas volume of 0.94 m^3 filled with nitrogen N_2 was used for the separation of pions, protons, and kaons in the K12 beam. The total amount of material in the beam path represents $3.5 \times 10^{-2} X_0$. The gas is kept at room temperature, and its pressure can be tuned between vacuum and 5 bar. The optimal value for the kaon identification is 1.75 bar. As shown in fig. 2.5, the particles mentioned above can be clearly distinguished. In the ongoing data taking of NA62, the nitrogen gas was replaced by hydrogen [28].

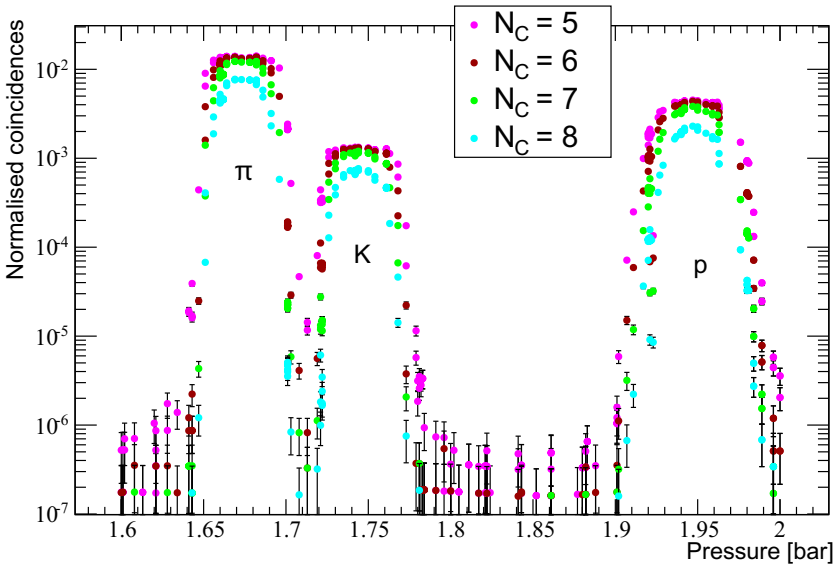

Figure 2.5: Results of a CEDAR pressure scan with N_2 radiator gas from 2015. The normalized number of events versus the N_2 pressure is plotted for various minimum number N_C of KTAG sectors in coincidence. The pion, kaon, and proton peaks are very well distinguishible. Figure from [9].

The KTAG kaon identification efficiency based on the $K^+ \to \pi^+\pi^0$ decays is found to be over 98% when requiring the coincidence in at least 5 sectors. The probability of misidentifying a pion as a kaon at the operating pressure is estimated as $O(10^{-4})$.

2.2.4 Beam Spectrometer (GTK)

The beam spectrometer measures the momentum, time, and direction of the incoming particles in the beam. The system consists of three stations composed of silicon pixel detectors installed around four dipole magnets in the beam vacuum. The particle momentum measurement is based on the vertical displacement of the trajectory in the second station. The system is designed to achieve the precision 0.2% when measuring the beam particle momentum and the angular precision of 16 μrad. The material for each station represents less than 0.5% X_0. The schematic layout is depicted in fig. 2.6.

The effect of using the information given by GTK instead of the nominal beam values can be seen in fig. 2.7 using the improved width (rms) of the m^2_{miss} distribution. The pion momentum P_π is measured by the Straw spectrometer.

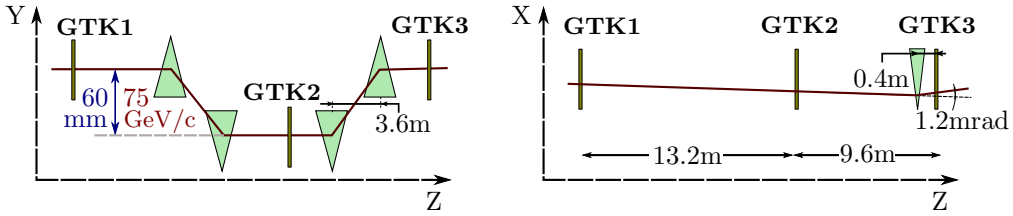

Figure 2.6: Schematic layout of the GTK system in the vertical and horizontal plane [9].

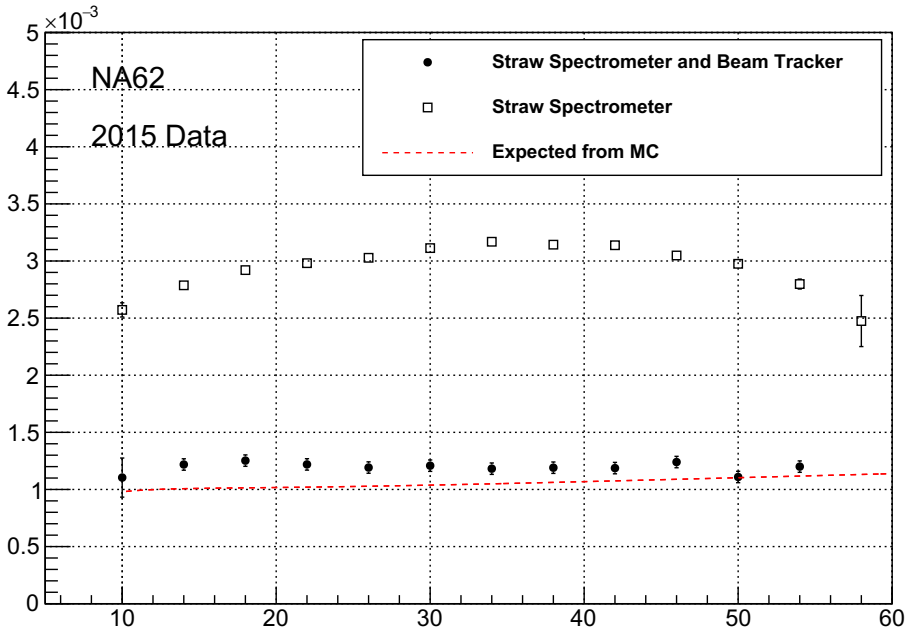

Figure 2.7: Standard deviation of the m^2_{miss} distribution of $K^+ \to \pi^+\pi^0$ events as a function of the pion momentum. The values based on the GTK output are represented by the black dots, while the values based on the nominal beam parameters by the open squares. Based on the data from 2015 [9].

2.2.5 Straw Spectrometer

The Straw spectrometer is used to measure the trajectories and momenta of charged kaon decay products. It is located 20 meters downstream of the decay region and comprises four straw chambers with a dipole magnet positioned between the first and the last two chambers (fig. 2.8). Each chamber consists of four views for measuring particle coordinates: X (0°), Y (90°), U (-45°), and V (45°). The basic characteristics of the Straw spectrometer are presented in table 2.2 and fig. 2.9.

The spectrometer consists of 7168 straws with a length of 2160 mm and a diameter of 9.82 mm placed in a vacuum. Each straw is filled with 70% of Ar and 30% of CO_2 at atmospheric pressure. Straws are made of 36 μm mylar, coated with 50 nm copper and 20 nm gold on the inside. The gold-plated tungsten anode wires are in the center of the straws. The total amount of material in the spectrometer corresponds to 1.8% X_0.

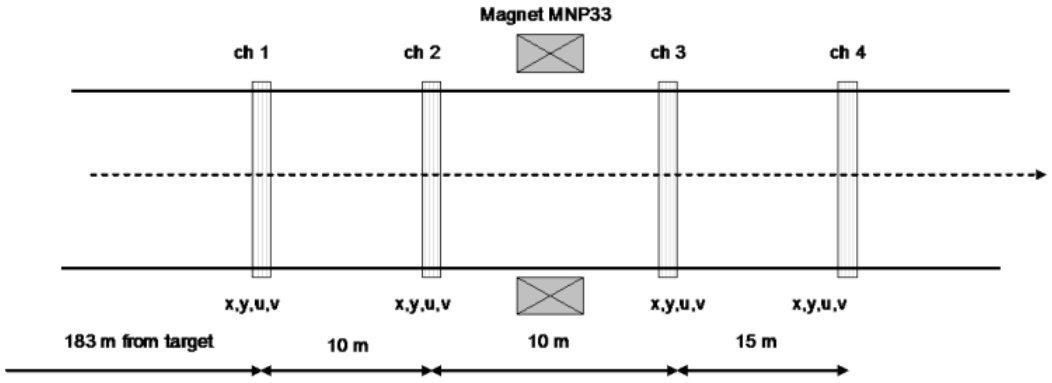

Figure 2.8: Schematic layout of the Straw spectrometer. The MNP33 magnet is placed between Chamber 2 and Chamber 3. Figure from [29].

Table 2.2: The basic Straw spectrometer characteristics. The spectrometer consists of 4 chambers (Chamber 1 – Chamber 4) and a large aperture dipole magnet MNP33 placed between Chamber 2 and Chamber 3. Table from [9].

Number of chambers:	4		
Number of views / chamber	4		
Order of views along beam direction	U, V, X, Y		
Number of straws per view	448		
Beam hole size (octagon apothem)	6 cm		
Beam Hole Offset	X	Y	Z
Chamber 1	101.2 mm	0 mm	183 m
Chamber 2	114.4 mm	0 mm	193 m
MNP33			198 m
Chamber 3	92.4 mm	0 mm	204 m
Chamber 4	52.8 mm	0 mm	218 m

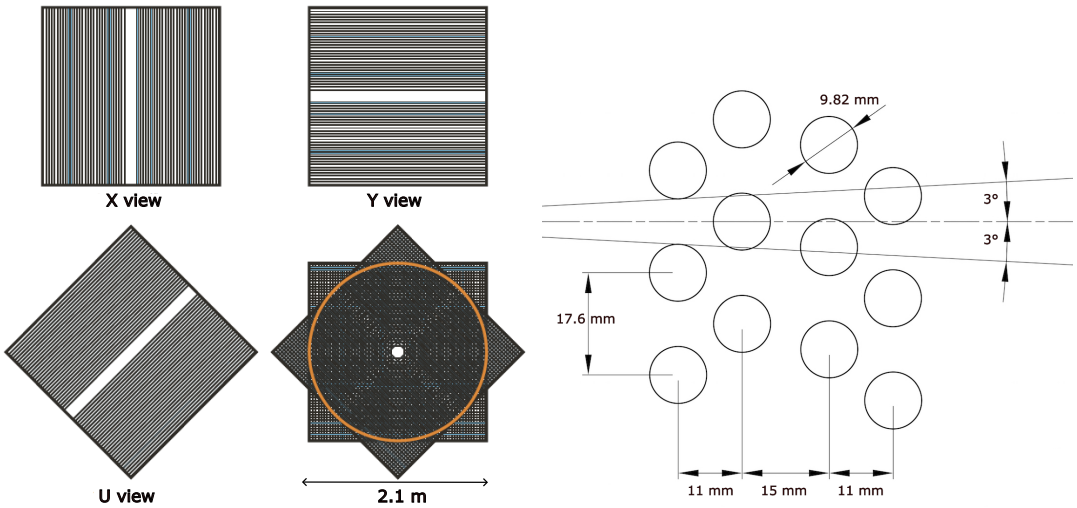

Figure 2.9: Left: View sections. A 12 cm wide gap in the middle of each view allows free passage of undecayed beam particles. Right: Straws are ordered to form four planes for each view. Figure from [9].

The source of the magnetic field within the Straw spectrometer is the magnet MNP33 of dimensions 2.3 m × 2.3 m × 1.3 m placed at the position $z = 197$ m (fig. 2.8). The magnet generates an integrated vertical field of 0.9 Tm, providing the momentum kick of 270 MeV/c in the x direction. The basic properties of the magnet are summarized in table 2.3.

Table 2.3: The main parameters of the field generated by MNP33 [9].

The measured field at the center of the magnet	0.38 T
Integrated field	0.9 Tm
Maximum field close to the poles	< 1.0 T
Transverse momentum kick	270 MeV/c
Effective magnetic length	2.13 m
Effective aperture diameter	2.37 m

As shown in fig. 2.10, the position resolution within a straw depends on the wire distance. The angular resolution of the spectrometer varies from 60 μrad at 10 GeV/c to 20 μrad at 50 GeV/c. The momentum resolution is

$$\frac{\sigma_p}{p} = 0.30\% \oplus 0.005\% \cdot p. \tag{2.2}$$

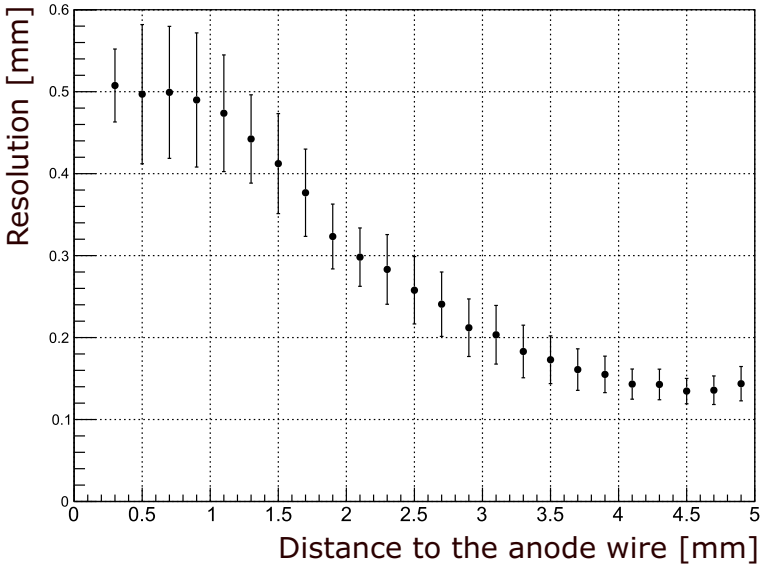

Figure 2.10: Particle position resolution as a function of the wire distance in a straw [29].

2.2.6 Liquid Krypton Calorimeter (LKr)

The liquid krypton calorimeter used in the NA62 experiment comes from the previous experiment NA48 [30]. It contains 9000 liters of liquid krypton at 120 K placed inside a cryostat. The material in the calorimeter corresponds to 27 X_0.

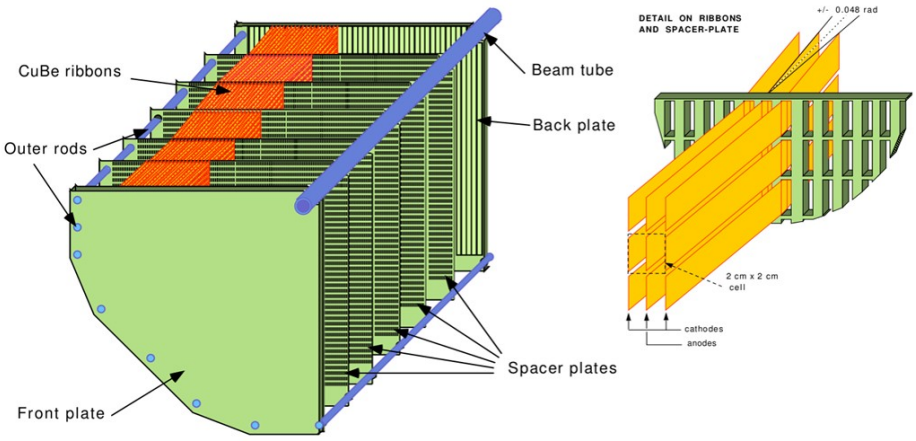

Figure 2.11: Left: schematic of the calorimeter structure (one quadrant). Right: detail of the calorimeter cells [9].

The sensitive area comprises 13 248 longitudinal cells with a cross-section of about 2×2 cm^2. The calorimeter is schematically depicted in fig. 2.11.

The energy, space, and time resolution of the calorimeter have been evaluated by NA48 [30]. The first estimation of the energy resolution obtained from simulated data in NA62 is

$$\frac{\sigma(E)}{E} = \frac{4.8\%}{\sqrt{E}} \oplus \frac{11\%}{E} \oplus 0.9\%, \tag{2.3}$$

where the energy is measured in GeV.

Clusters of energy E_{clus} are formed from a seed, which is any cell with energy E_{seed} above 250 MeV and greater than the sum of energies in the eight neighboring cells. These clusters include all cells within 11 cm of the cluster center, defined as the energy-weighted position of the participating cells. A track is associated if its impact point on the calorimeter front face coincides with the cluster position within 15 cm. A photon candidate is defined as an energy cluster without an associated track.

2.2.7 Ring Imaging Cherenkov Counter (RICH)

The RICH detector is used for the separation of pions and muons between momenta of 15 and 35 GeV/c, which gives a muon suppression factor of at least 100 for the $K^+ \to \pi^+\nu\overline{\nu}$ measurement. The RICH provides quite a good time resolution (100 ps), so the time of the charged track measured by the RICH can be used as a reference time (fig. 2.13).

The RICH radiator is a 17.5 m long cylindrical vessel with a gradually decreasing diameter from 4.2 m to 3.2 m. The vessel material is ferro-pearlitic steel, and the filling is neon gas. The photon detection system consists of approximately 2000 PMs and is placed in the detector's front part. Twenty spherical mirrors reflecting the Cherenkov light cone into a ring on the PM array are situated in the detector's back part. The RICH detector is schematically depicted in fig. 2.12.

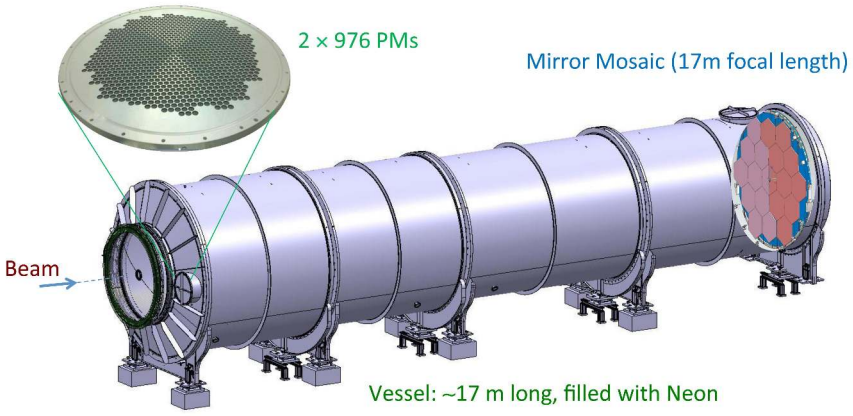

Figure 2.12: RICH schematic view. A zoom on one of two disks carrying the PMs is shown on the left. The mirror mosaic can be seen on the right [9].

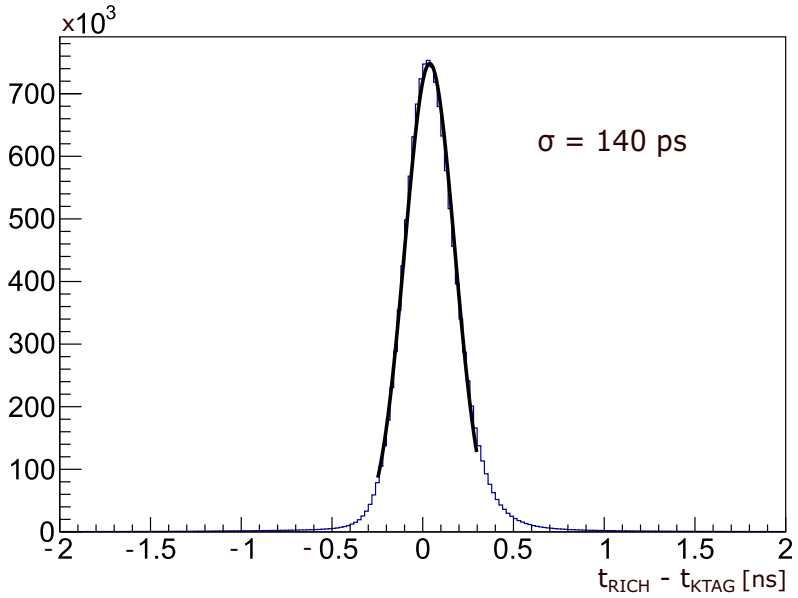

Figure 2.13: The time difference between the average time of a Cherenkov ring and the KTAG time. The Gaussian width is 140 ps. The data from 2014 and 2015 used [9].

2.2.8 Charged Particle Hodoscopes

Charged particle hodoscopes is a scintillator detector system covering the lateral acceptance downstream of the RICH and upstream of the LKr calorimeter given by the LAV12 detector inner radius (1070 mm) and the IRC detector outer radius

(145 mm). The main purpose is to provide input for the L0 trigger. The system consists of the NA48-CHOD detector located downstream of the LAV12 and the CHOD detector placed upstream of the LAV12.

NA48-CHOD detector

The NA48-CHOD is formed by two consecutive planes of 64 vertical and 64 horizontal BC408 plastic scintillator slabs of 20 mm (0.1 X_0) thickness. The vertical and horizontal slabs measure independently. The 128 counters are arranged into four quadrants of 16 slabs in each plane. Slab lengths vary from 1210 mm (inner slabs) to 600 mm (outer slabs), and the widths from 65 mm to 99 mm. The NA48-CHOD layout is depicted in fig. 2.14. The NA48-CHOD provides L0 trigger signals and reference time for events with charged particles in the final state. The time difference distribution between a NA48-CHOD track signal and the KTAG beam kaon candidate is displayed in fig. 2.15.

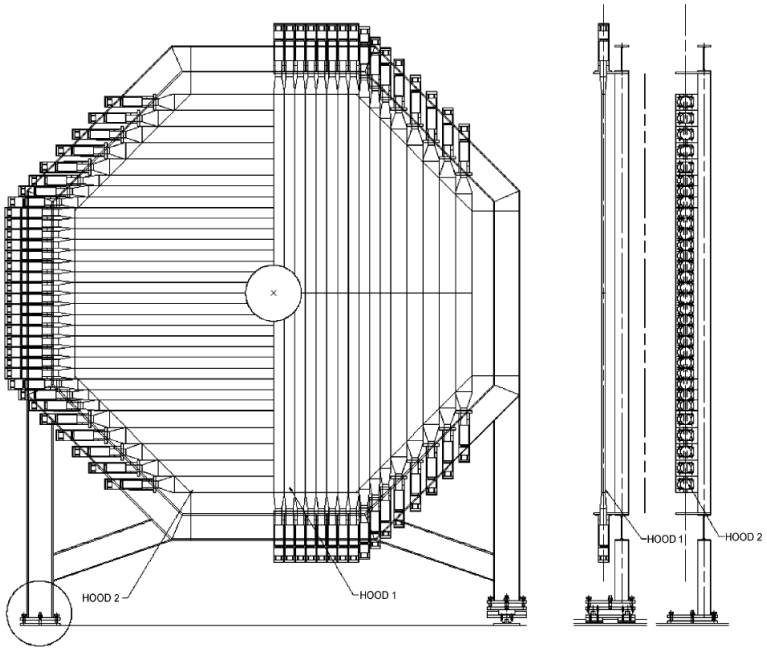

Figure 2.14: Schematic of the NA48-CHOD detector [9].

CHOD detector

The CHOD active area contains 152 horizontal plastic scintillator tiles of 30 mm thickness covering an annulus with an inner radius of 140 mm and an outer radius of 1070 mm. Different tile groups can be considered to form specific trigger requirements. The tile width is mostly 108 mm, and lateral tiles are 134 mm or 268 mm wide. The vertical spaces between the tile centers are 107 mm, which means a 1 mm overlap; the rows of tiles are placed alternatively on the sides of a 3 mm thick central support foil. The total material thickness in the active area corresponds to 0.13 X_0. The CHOD layout is shown in fig. 2.16. The expected time resolution of the CHOD signals is of $O(1\text{ ns})$.

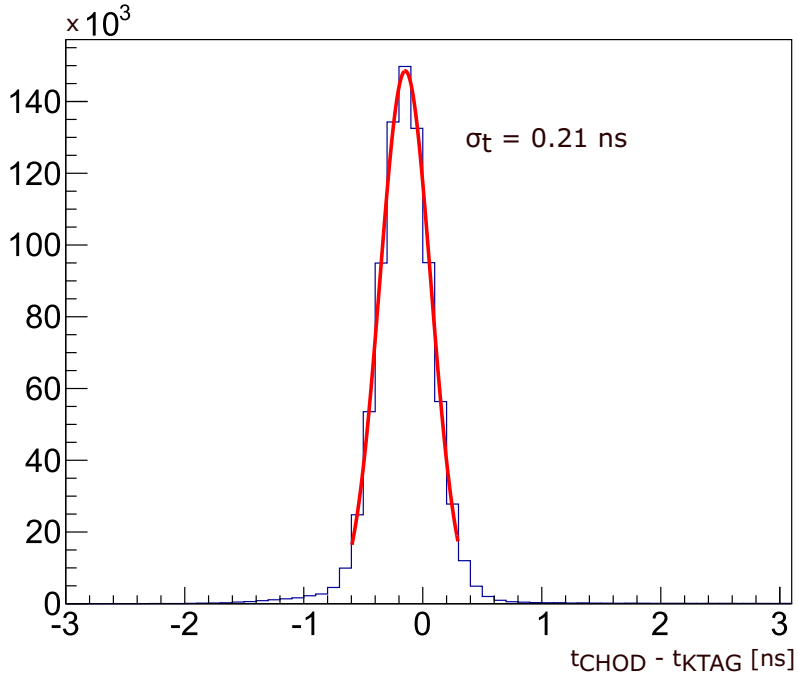

Figure 2.15: Time difference between the NA48-CHOD candidate and KTAG kaon signal. Obtained from data recorded at 1% nominal beam intensity in 2015 [9].

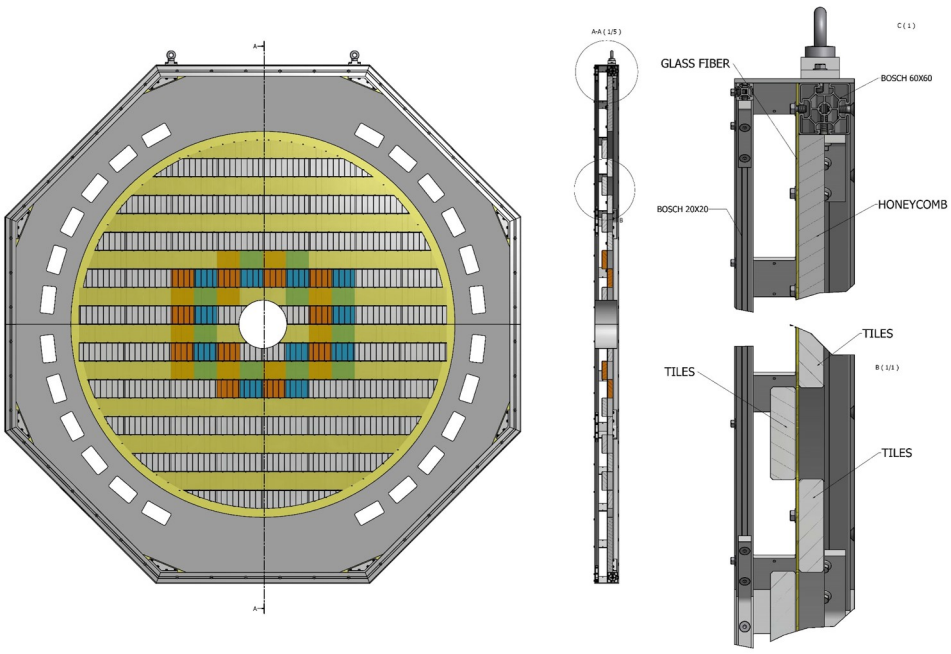

Figure 2.16: The schematic of the CHOD detector (left). The G10 support panel (bottom right) carries the scintillator tiles. The structure is stiffened with honeycomb and aluminum construction profiles (top right). The detector's active area is divided into four quadrants [9].

2.2.9 Trigger System

The text in this section is inspired by the publication [31] describing the NA62 trigger system performance.

The trigger system at NA62 comprises two stages. The first stage is a low-level hardware trigger (L0) that processes data from detectors using the electronics and forms an L0 trigger decision. The second (high-level) stage, L1, is a software trigger running on a dedicated data-acquisition computing cluster (DAQ farm).

A trigger line is defined by a sequence of L0 and L1 trigger conditions, aiming to select specific types of events. There are multiple trigger lines defined during the NA62 data taking. An event is stored on disk if at least one of the trigger lines is satisfied. In the presented analysis, we use the electron multi-track (eMT) line collecting K^+ decays to multi-electron final states. The trigger lines are listed in table 2.4, and the individual conditions involved in the eMT line are described in the following text. Each trigger line can be scaled down to reduce its bandwidth. The eMT line was downscaled by factor 8 for most of the 2017–2018 data taking.

Table 2.4: K^+ trigger lines and the corresponding L0 and L1 trigger conditions. An overline indicates that the condition is used in the veto. The eMT trigger is used in the signal and normalization selection. Table from [31].

Trigger line	**L0 trigger conditions**	**L1 trigger conditions**
PNN	RICH · Q1 · UTMC · $\overline{\text{QX}}$ · $\overline{\text{M1}}$ · $\overline{\text{LKr30}}$	KTAG · $\overline{\text{LAV}}$ · STRAW
Non-μ	RICH · Q1 · $\overline{\text{M1}}$	KTAG · STRAW-1TRK
MT	RICH · QX	KTAG · STRAW-Exo
2μMT	RICH · QX · MO2	KTAG · STRAW-Exo
***e*MT**	**RICH · QX · E20**	**KTAG · STRAW-Exo**
μMT	RICH · QX · MO1 · E10	KTAG · $\overline{\text{LAV}}$ · STRAW-MT
DV-μ	RICH · Q2 · MO1 · E10	$\overline{\text{KTAG}}$ · STRAW-DV
DV-2μ	RICH · Q2 · MO2 · $\overline{\text{E10}}$	STRAW-DV
Neutrino	RICH · Q1 · MOQX · $\overline{\text{Q2}}$	KTAG · $\overline{\text{LAV}}$ · STRAW-1TRK
Control	NA48-CHOD	None

The L0 Trigger System

The full list of L0 conditions available at NA62 during the 2016–18 data taking are summarized in table 2.5. The conditions forming the electron multi-track trigger line used in this analysis are based on information from RICH, CHOD, and LKr detectors. The RICH condition requires at least two hits registered by the detector. The CHOD condition, named QX, requires the coincidence of signals from two diagonally opposite quadrants shown in fig. 2.16. The LKr condition (E20) requires at least 20 GeV of energy to be deposited in the calorimeter.

The L1 Trigger System

The online framework comprises the DAQ and high-level trigger (HLT) software. The data from most of the detectors are sent to the DAQ farm following a positive L0 decision, and an L0 event is produced. The L1 trigger algorithms then process

Table 2.5: List of L0 trigger conditions. The LKr conditions differ between K^+ and beam-dump configuration. The RICH, QX, and E20 conditions are part of eMT trigger used in the signal and normalization selection. Table from [31].

Detector	Condition	Description
RICH	**RICH**	**At least two signals in the detector**
CHOD	Q1	At least one signal in any quadrant
	Q2	At least one signal in each of two different quadrants
	QX	**At least one signal in each of two diagonally-opposite quadrants**
	UTMC	Upper multiplicity condition: fewer than five signals in the detector
NA48-CHOD	NA48-CHOD	At least one signal in any quadrant
MUV3	M1	At least one signal in the detector
	MO1	At least one signal in the outer tiles
	MO2	At least two signals in the outer tiles
	MOQX	At least one signal in each of two diagonally-opposite quadrants
LKr	E10	At least 10 GeV deposited in the LKr
	E20	**At least 20 GeV deposited in the LKr**
	E30	At least 30 GeV deposited in the LKr
	C2E5	At least 5 GeV deposited in the LKr by at least two clusters
	LKr30	Logical OR between E30 and C2E5
LKr	E1	At least 1 GeV deposited in the LKr
(beam dump)	E2	At least 2 GeV deposited in the LKr
	E4	At least 4 GeV deposited in the LKr
	C2E2	At least 2 GeV deposited in the LKr by at least two clusters

the event. If the event satisfies the L1 trigger requirements, the data from the remaining detectors are requested to produce a complete event. The electron multi-track trigger L1 conditions use the information produced by the KTAG and Straw-Exo algorithms.

The L1 KTAG trigger looks for a signal consistent with a K^+ in time with the L0 trigger. This rejects the events triggered at L0 by halo muons and scattered beam pions. The trigger requires at least five KTAG sectors to have at least one detected Cherenkov photon within 5 ns of the L0 trigger time.

The L1 Straw trigger reconstructs the charged tracks passing the Straw detector in time with the L0 trigger. The track momenta must be at least 3 GeV/c, and the track slopes must satisfy $|dX/dZ| < 0.02$ and $|dY/dZ| < 0.02$. The fake tracks are suppressed by applying quality conditions on the signal and track times. Furthermore, the selection requires the track momenta below 50 GeV/c and the closest distance of approach (CDA) of a track to the nominal beam axis below 200 mm with the CDA position upstream of the first straw chamber. Multi-track events are associated with CDA between two tracks below 30 mm. The L1 Straw-Exo requires at least one negatively charged track.

2.2.10 Software Framework

The NA62 software framework [32] comprises three main packages:

1. NA62MC: Monte Carlo (MC) simulations of particle interactions with the detector and its response based on the Geant4 toolkit [33].

2. NA62Reconstruction: Processing of both real and simulated data that produces reconstructed quantities such as tracks with momenta (for spectrometers) or clusters (for calorimeters).

3. NA62Analaysis: Tools and routines used to perform data analysis tasks.

3. The π^0 Double Dalitz Decay Branching Ratio Measurement at the NA62

3.1 Analysis Overview

In the NA62 experiment, the high-intensity kaon beam (section 2.2.2) is produced. As shown in table 1.2, four out of six main K^+ decay channels have at least one π^0 in the final state, which means that the NA62 experiment can also be used for the study of π^0 decays. For the presented analysis, the most suitable channel to select neutral pions is $K^+ \to \pi^+\pi^0$ since it has the biggest branching ratio and no neutrino in the final state, which makes it possible to detect all final-state particles.

The analysis uses data collected by NA62 from 2017 to 2018 (Run 1). The experiment resumed its data taking in 2021 (Run 2) with various improvements of the trigger system (section 2.2.9), which resulted in lower downscaling factors for the electron multi-track trigger line. As a result of the development, the NA62 should increase the size of the di-electron data sample by about a factor of ten. The aim of this analysis is to perform the first π^0 double Dalitz decay branching ratio measurement at NA62 using the Run 1 data set, including some of the systematics studies, most importantly, the track reconstruction efficiency.

Events are selected from the data sample filtered by the RES3TV filter, which selects events with at least one good three-track vertex. Bad bursts and bad events are rejected for CEDAR, Spectrometer, RICH, CHOD, NA48-CHOD, and LKr systems. The Monte Carlo (MC) samples are used to model the signal, normalization, and backgrounds from individual K^+ decays. The MC samples also include a simulation of pile-up activity in the detectors. The analysis uses analyzers developed for this thesis and also common analyzers and algorithms from the NA62 framework [32].

The branching ratio of a given decay channel is the probability that the given channel occurs. In our analysis, the branching ratio of the inclusive π^0 double Dalitz decay $B(\pi^0 \to e^+e^-e^+e^-(\gamma),\ x_{4e} > 0.9)$ is measured, where x_{4e} is defined by eq. (1.5). The value of $x_{4e} = 0.9$ corresponds to the four-electron invariant mass value of $m_{eeee} \approx 128.1$ MeV/c^2. The signal channel is the $K^+ \to \pi^+\pi^0$ decay followed by the $\pi^0 \to e^-e^+e^-e^+(\gamma)$ decay denoted in the following text as $\pi^0_{DD(\gamma)}$. The branching ratio of this channel can be factorized as

$$B(K^+ \to \pi^+\pi^0_{DD(\gamma)}) = B(K^+ \to \pi^+\pi^0)B(\pi^0_{DD(\gamma)}). \tag{3.1}$$

The branching ratio of the signal channel could be, in principle, computed from the total number of signal events occurring in the fiducial decay region $N(K^+ \to \pi^+\pi^0_{DD(\gamma)})$ and the total number of kaon decays N_K:

$$B(K^+ \to \pi^+\pi^0_{DD(\gamma)}) = \frac{N(K^+ \to \pi^+\pi^0_{DD(\gamma),})}{N_K}. \tag{3.2}$$

However, the problem is that neither the numerator nor the denominator in the eq. (3.2) is known. The number of observed signal events N_{sig} in the data sample is not equal to $N(K^+ \to \pi^+\pi^0_{DD(\gamma)})$ because not all signal events are detected, e.g., due to final-state particles not crossing the active volume of detectors used in the selection procedure. This fact is corrected for by using MC samples from which the so-called acceptance is evaluated as:

$$A(K^+ \to \pi^+\pi^0_{DD(\gamma)}) = \frac{M_{\text{sig}}}{M_{\text{sig}}^{\text{ACC}}}, \tag{3.3}$$

where M_{sig} is the number of signal events selected from the simulated $K^+ \to \pi^+\pi^0_{DD(\gamma)}$ MC sample and $M_{\text{sig}}^{\text{ACC}}$ is the number of generated signal events with the vertex z position in the interval (105, 180) m and with $x_{4e} > 0.9$. Using the assumption that the simulation reproduces the acceptance effects present also in the real data, we obtain the corrected number of signal events by dividing N_{sig} by the acceptance.

An auxiliary selection of a normalization channel is used to get the total number of decayed kaons N_K. For the normalization channel, it is assumed that the branching ratio is known and the number of N_K is computed using an equation analogous to eq. (3.2) and the same considerations about the acceptance as for the signal. The normalization channel should be as similar to the signal one as possible to cancel systematic effects, such as different efficiencies in data and MC. Unfortunately, there is no K^+ decay channel with five charged particles in the final state with a branching ratio larger than $B(K^+ \to \pi^+\pi^0_{DD(\gamma)})$. In our analysis, we decided to use the decay channel $K^+ \to \pi^+e^+e^-$ for normalization since it contains one electron-positron pair in the final state, which allows us to use the same trigger line for both signal and the normalization. As a result, an important systematic effect originating from different track reconstruction efficiency in data versus MC for five- and three-track events (signal vs. normalization) is introduced.

Additionally, background may contribute to the number of observed events in both the signal and the normalization samples. The formula for the number of observed events then becomes:

$$N_{\text{sig (norm)}} = N_K \sum_{\text{MC samples}} B_i A_i, \tag{3.4}$$

where A_i and B_i are acceptances and branching ratios of various MC samples contributing to either signal or normalization.

The possible backgrounds for the signal are $K^+ \to \pi^0_{DD}e^+\nu_e$, $K^+ \to \pi^0_{DD}\mu^+\nu_\mu$, $K^+ \to \pi^+\pi^0_D$ (plus external photon conversion) and for the normalization $K^+ \to \pi^+\pi^0_{DD(\gamma)}$ and $K^+ \to \pi^+\pi^0_D$. As discussed in section 3.3 and section 3.4, all the mentioned backgrounds are negligible. Therefore, a simple formula can be derived for the measured branching ratio:

$$B(\pi^0_{DD(\gamma)}) = \frac{N_{\text{sig}}}{N_{\text{norm}}} \frac{A(K^+ \to \pi^+e^+e^-)B(K^+ \to \pi^+e^+e^-)}{A(K^+ \to \pi^+\pi^0_{DD(\gamma)})B(K^+ \to \pi^+\pi^0)}. \tag{3.5}$$

3.2 The $K^+ \to \pi^+\pi^0_{DD(\gamma)}$ MC Generator

The MC generator of the decay $\pi^0_{DD(\gamma)}$ has recently been developed by Tomáš Husek for NA62. The reason for the development was our finding that the previous version of the NA62 π^0_{DD} generator did not include extra photon radiation and did not describe the spectra observed in the data sufficiently. This section summarizes the new generator development as reported by Tomáš Husek internally to the NA62 collaboration [26].

For our measurement, it is necessary to include radiative corrections and generate events with radiative photons in the final state as it was done for the KTeV measurement (section 1.4). Since we aim to measure the inclusive branching ratio with a cutoff $x_{4e} > 0.9$ (section 1.3.1), it is necessary to simulate radiative events in a wider range than the region of interest due to resolution effects. The new $\pi^0_{DD(\gamma)}$ MC generator produces events with $x_{4e} > 0.8$ (or $m_{eeee} > 120.7$ MeV/c^2). The contributions of the two-photon exchange diagram fig. 1.4a were computed in the soft-photon limit, which was validated to be correct in the restricted range $x_{4e} > 0.8$.

The branching ratio of inclusive π^0 double Dalitz decay with $x_{4e} > x^{\text{cut}}_{4e}$ (soft-photon region) can be expressed as

$$\begin{aligned} B(\pi^0_{DD(\gamma)}, x_{4e} > x^{\text{cut}}_{4e}) &= \left[1 + \delta(x^{\text{cut}}_{4e})\right] B(\pi^0_{DD}), \\ \delta(x^{\text{cut}}_{4e}) &= -0.1727(2) + 0.0411(1) \log \frac{1 - x^{\text{cut}}_{4e}}{0.0015}, \end{aligned} \tag{3.6}$$

where $B(\pi^0_{DD})$ represents the leading-order (four-body) process branching ratio. The $\delta(x^{\text{cut}}_{4e})$ dependence on the certain x^{cut}_{4e} values and the corresponding maximal energy of the irradiated photon $E^{*\text{max}}_{\gamma}$ is given in table 3.1.

Table 3.1: The $\delta(x^{\text{cut}}_{4e})$ correction function. Table from [26].

$E^{*\text{max}}_{\gamma}$	0.1	1.0	3.375	6.749
x^{cut}_{4e}	0.9985	0.9852	0.95	0.90
$\delta(x^{\text{cut}}_{4e})$ [%]	-17.27(2)	-7.86(4)	-2.86(6)	0.01(6)

The 1PE diagrams are not involved in the MC generator since the corresponding events have small values of $x_{4e} < 0.8$ and do not contribute to our measurement. The theory also predicts that the 1PE topology contributed to the total inclusive rate by approximately 0.6%. As the 2PE contribution diverges for $x_{4e} \to 1$, generation of such events is done in the limited range $x_{4e} < 0.9852$ (or $m_{eeee} < 134$ MeV/c^2). This means that the events with $0.8 < x_{4e} < 0.9852$ are generated as 5-body decays and the events with $x_{4e} > 0.9852$ as 4-body decays (without an extra radiative photon). The probability ratio of 5-body to 4-body decays is

$$R_{5/4}(0.9852) = \frac{B(\pi^0_{DD\gamma}, x_{4e} < 0.9852)}{B(\pi^0_{DD(\gamma)}, x_{4e} > 0.9852)} \approx 10.5\%. \tag{3.7}$$

In the first step, the $\pi^0_{DD(\gamma)}$ MC generator algorithm randomly selects if the event will be generated as the 4-body or 5-body event. The choice is done according to the probability ratio $R_{5/4}$ (eq. (3.7)). Four-momenta of final-state particles

with a certain weight w is generated using the TGenPhaseSpace class[1] and the corresponding squared matrix element $|M|^2$ is computed. Maximal weight $w_{\max}$ and maximal square root matrix element $|M|^2_{\max}$ were determined beforehand for both 4- and 5-body events. The accept/reject method then samples events according to the matrix element squared. The m_{eeee} distribution evaluated using the $K^+ \to \pi^+\pi^0_{DD(\gamma)}$ MC truth information is shown in fig. 3.1.

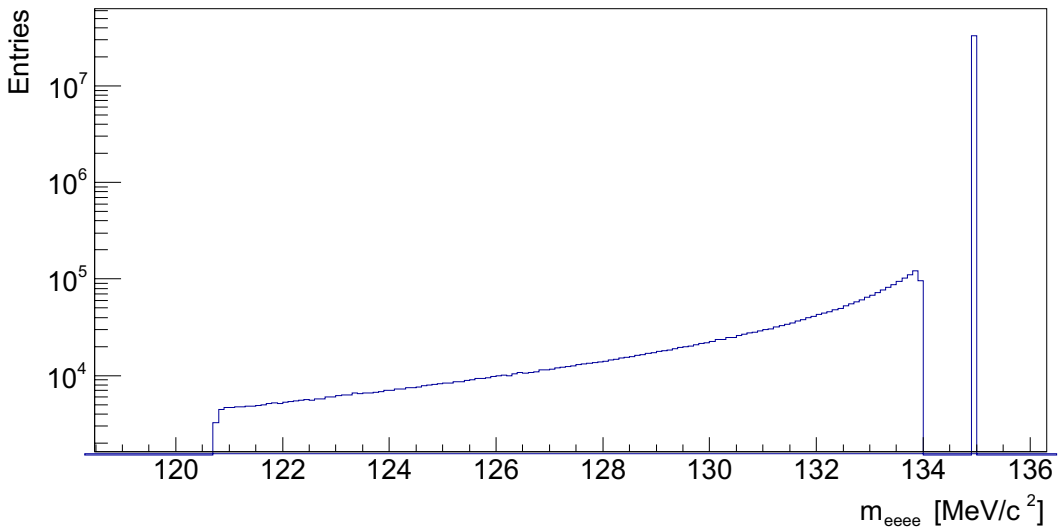

Figure 3.1: The m_{eeee} distribution in logarithmic scale obtained from $\pi^0_{DD(\gamma)}$ MC truth information. The continuous part of m_{eeee} distribution corresponds to the region $0.8 < x_{4e} < 0.9852$ (or 120.7 MeV/c^2 $< m_{eeee} <$ 134 MeV/c^2). Signal events with reconstructed m_{eeee} larger than 125 MeV/c^2 are selected in the analysis (section 3.3.2).

3.3 Signal Selection

The $K^+ \to \pi^+\pi^0_{DD}$ is characterized by five particles in the final state – a positively charged pion and two electron-positron pairs. Since the π^0 mean free path at NA62 is only a few μm, the signal event is associated with a vertex consisting of five reconstructed charged tracks – three positive and two negative (fig. 3.2a). The five-track vertex selection is described in section 3.3.1.

A possible background to the signal could originate from the decay $K^+ \to \pi^+\pi^0_D$, where π^0_D stands for the Dalitz decay $\pi^0 \to e^+e^-\gamma$. Two extra tracks could be produced with an external photon conversion in a material. However, the NA62 decay region and the Straw Spectrometer are located in a vacuum ($p < 10^{-5}$ mBar). Therefore, the photon conversions can occur only in the Straw detector material as shown in fig. 3.2b. The main cut suppressing such events is the track separation in the Straw chambers (section 3.3.1).

The particle identification in the final state is based only on the kinematics to avoid the loss of acceptance (section 3.3.2). The signal selection uses the multi-track electron trigger described in section 2.2.9.

[1] https://root.cern.ch/doc/master/classTGenPhaseSpace.html

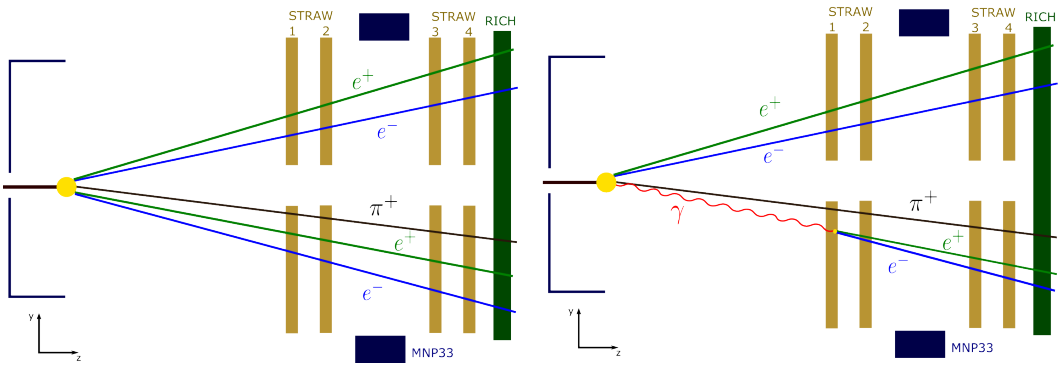

(a) Five-track vertex in a signal event. (b) Photon conversion in Straw.

Figure 3.2: A schematic view of a $K^+ \to \pi^+\pi^0_{DD}$ signal event (left) and a possible $K^+ \to \pi^+\pi^0_D$ background event (right).

3.3.1 Five-track Vertex Selection

This section is inspired by the publication [34] focused on the $K^+ \to \pi^+e^+e^-e^+e^-$ decay search at NA62, where the $K^+ \to \pi^+\pi^0_{DD}$ decay was used as the normalization channel. The cuts associated with the five-track vertex selection are summarized in the following steps:

- The events containing exactly one five-tack vertex with charge $q = +1$ are selected. The vertex has to occur in the decay region so its longitudinal position satisfies 105 m $< z_{\text{vtx}} <$ 180 m.
- The vertex quality parameter should be $\chi^2 < 25$.
- The distance between the vertex and the beam axis should be smaller than 40 mm. The distance between each track and the beam axis should not exceed 50 mm.
- Each track is required to be in the Straw geometric acceptance as shown in fig. 3.2a.
- To suppress the possible background caused by the π^0_D events with the photon conversion in the Straw detector (fig. 3.2b), the separation between track pairs is required to be more than 15 mm in the transversal planes of all Straw chambers.
- For each track, the momentum should belong to the interval (7, 45) GeV/c with the quality requirement $\chi^2 < 40$.
- The momentum conservation law leads to cuts on the vertex momentum magnitude and its transverse momentum. The cut on momentum excess is $|\Delta p| < 2$ GeV/c with $\Delta p = p_{\text{vtx}} - p_{\text{beam}}$ defined as the momentum magnitude difference between the vertex and the beam. The total transverse momentum of the tracks with respect to the beam is $p_T < 25$ MeV/c.
- The track times measured by Straw must satisfy $|t_{\text{Straw}} - t_{\text{trigger}}| < 20$ ns, where t_{trigger} is the event trigger time.

- To identify the signal event, the cuts on the four-electron invariant mass and the total invariant mass are applied. The procedure is described in the following section.

- The multi-track electron trigger selecting di-electron final states described in section 2.2.9 is used to select data events. Therefore, the offline QX condition with a time window of 4 ns (coincidence time between hits in opposite CHOD quadrantes) and the offline E20 condition (total energy in the LKr over 20 GeV) are applied to match the trigger criteria. Additionally, the QX configuration is checked by the requirement that at least two tracks are in the CHOD acceptance and the corresponding hits occur in the diagonally opposite CHOD quadrants. For MC, emulated individual trigger conditions forming the trigger line are applied.

3.3.2 Particle Identification and Selected Samples

The final state of the signal event is formed by three positive tracks and two negative tracks. The particle identification (PID) task is to assign the correct mass (identity) to these tracks. Particle identification based on the downstream detectors, such as LKr, would be inefficient because of the loss of acceptance. Therefore, kinematic particle identification is used for this analysis.

Since the two electron-positron pairs come from the π^0_{DD}, the four-electron invariant mass m_{eeee} should be equal to the π^0 mass m_{π^0}. All particles in the final state originate from K^+; their invariant mass $m_{\pi eeee}$ should be equal to the K^+ mass m_K. Therefore, it is convenient to define the discriminant D as

$$D = \frac{(m_{\pi eeee} - m_K)^2}{\sigma^2_{m_{\pi eeee}}} + \frac{(m_{eeee} - m_{\pi^0})^2}{\sigma^2_{m_{eeee}}}, \tag{3.8}$$

where $\sigma_{m_{\pi eeee}}$ and $\sigma_{m_{eeee}}$ are standard deviations of the corresponding invariant mass distributions. By performing a Gaussian fit of the distributions obtained from Run 1 data, we get $\sigma_{m_{\pi eeee}} = 2.3$ MeV/c^2 and $\sigma_{m_{eeee}} = 1.2$ MeV/c^2. The resolution is well reproduced by MC simulation.

The negatively charged tracks from the 5-track vertex are assumed to be electrons. The task is to decide which of the three positive tracks is the π^+ (the remaining two positive tracks are therefore matched with positrons). This means that there are totally three options for particle identification. The correct particle identification corresponds to the option with the minimal value of D (eq. (3.8)). For this option, the $m_{\pi eeee}$ versus m_{eeee} 2D plot is displayed in fig. 3.3.

Finally, the invariant mass cuts are set as 484 MeV/$c^2 < m_{\pi eeee} <$ 504 MeV/c^2 and $|m_{eeee} - m_{\pi^0}| < 10$ MeV/c^2.

The number of $K^+ \to \pi^+\pi^0_{DD(\gamma)}$ events observed in Run 1 data is $N_{\text{sig}} = 1143$ and in the $K^+ \to \pi^+\pi^0_{DD(\gamma)}$ MC sample $M_{\text{sig}} = 8098$. The number of events with the vertex z position in (105, 180) m and $x_{4e} > 0.9$ is $M^{\text{ACC}}_{\text{sig}} = 34\ 334\ 648$. The possible backgrounds are $K^+ \to \pi^0_{DD}e^+\nu_e$ with a number of selected events 9 out of 18 334 450, $K^+ \to \pi^0_{DD}\mu^+\nu_\mu$ with a number of selected events 25 out of 18 998 080, and finally the $K^+ \to \pi^+\pi^0_D$ with no selected event out of 80 892 417. The signal selection acceptance $A(K^+ \to \pi^+\pi^0_{DD(\gamma)})$ and the background acceptances given by eq. (3.3) are

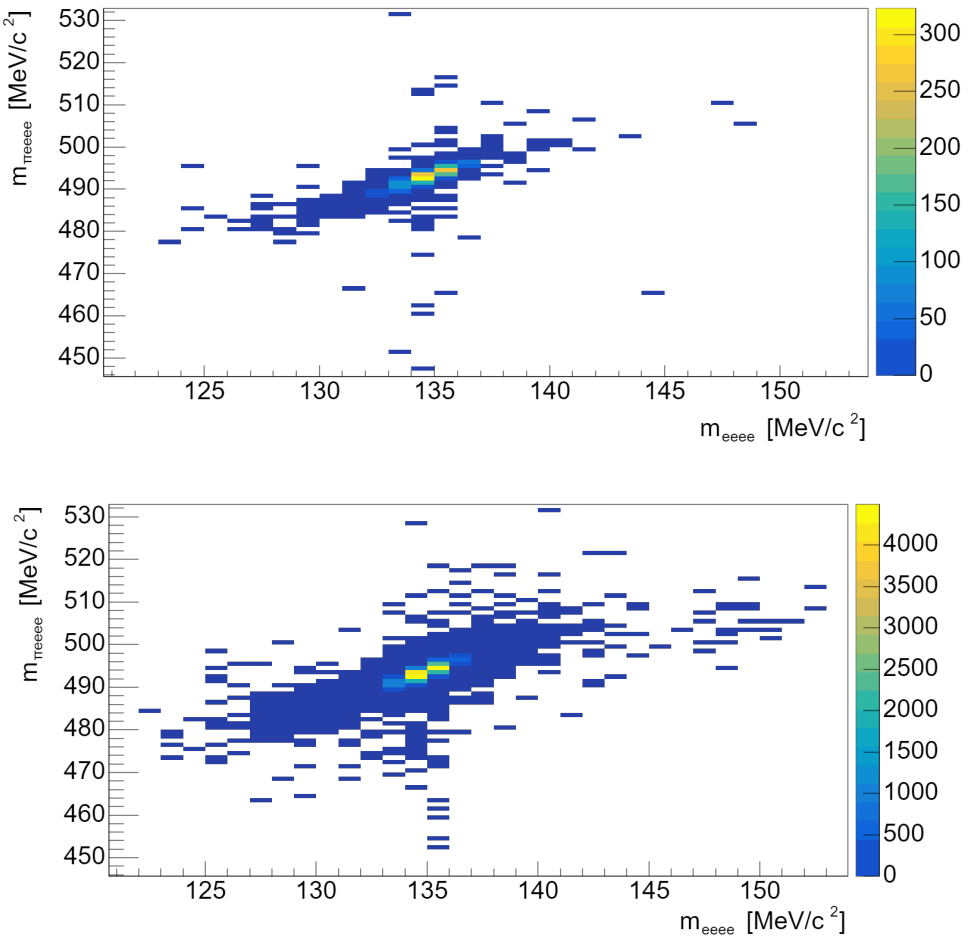

Figure 3.3: The $m_{\pi eeee}$ versus m_{eeee} for the best PID option. Plots obtained from the Run 1 data (top) and the signal MC simulation (bottom).

$$
\begin{aligned}
A(K^+ \to \pi^+ \pi^0_{DD(\gamma)}) &= (2.359 \pm 0.026) \times 10^{-4}, \\
A(K^+ \to \pi^0_{DD} e^+ \nu_e) &= (4.91 \pm 1.64) \times 10^{-7}, \\
A(K^+ \to \pi^0_{DD} \mu^+ \nu_\mu) &= (1.32 \pm 0.26) \times 10^{-6}.
\end{aligned}
\tag{3.9}
$$

The acceptances of the background processes are more than 100 times smaller than the signal acceptance, and their branching ratios are also smaller than the expected signal branching ratio. Therefore, backgrounds in the signal sample can be neglected.

The m_{eeee}, $m_{\pi eeee}$ distributions are shown in fig. 3.4. The particle momentum distributions are displayed in fig. 3.5. Since two electrons and two positrons occur in the final state, the momentum distributions are shown separately for higher-momentum and lower-momentum electrons and positrons. A significant discrepancy (a shift) between data and MC is observed in the π^+ momentum spectrum, which could be related to track reconstruction efficiency discussed later in the text.

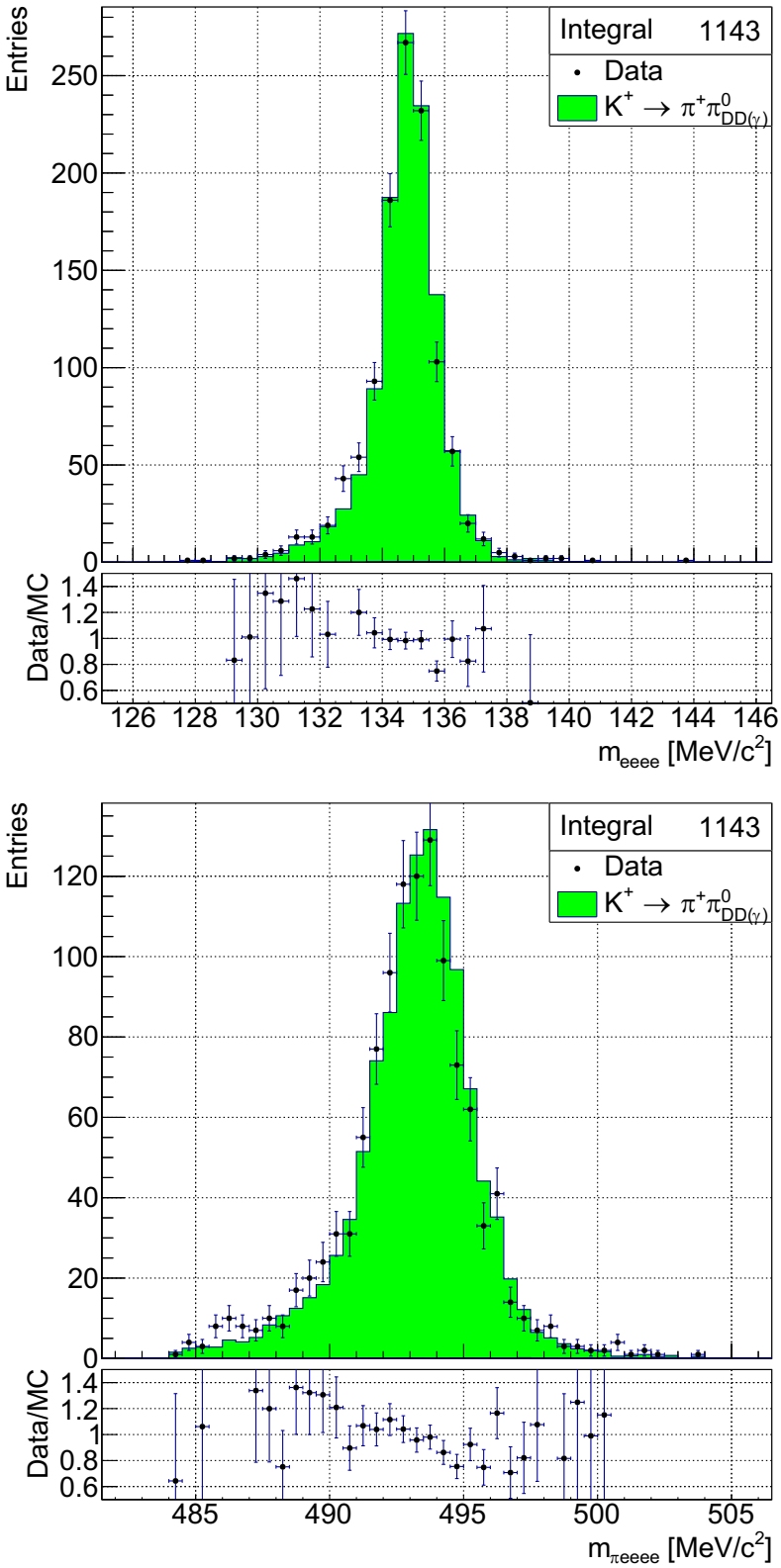

Figure 3.4: The m_{eeee} (top) and $m_{\pi eeee}$ (bottom) invariant mass distributions for the signal selection obtained from Run 1 data and the $K^+ \to \pi^+\pi^0_{DD(\gamma)}$ MC sample.

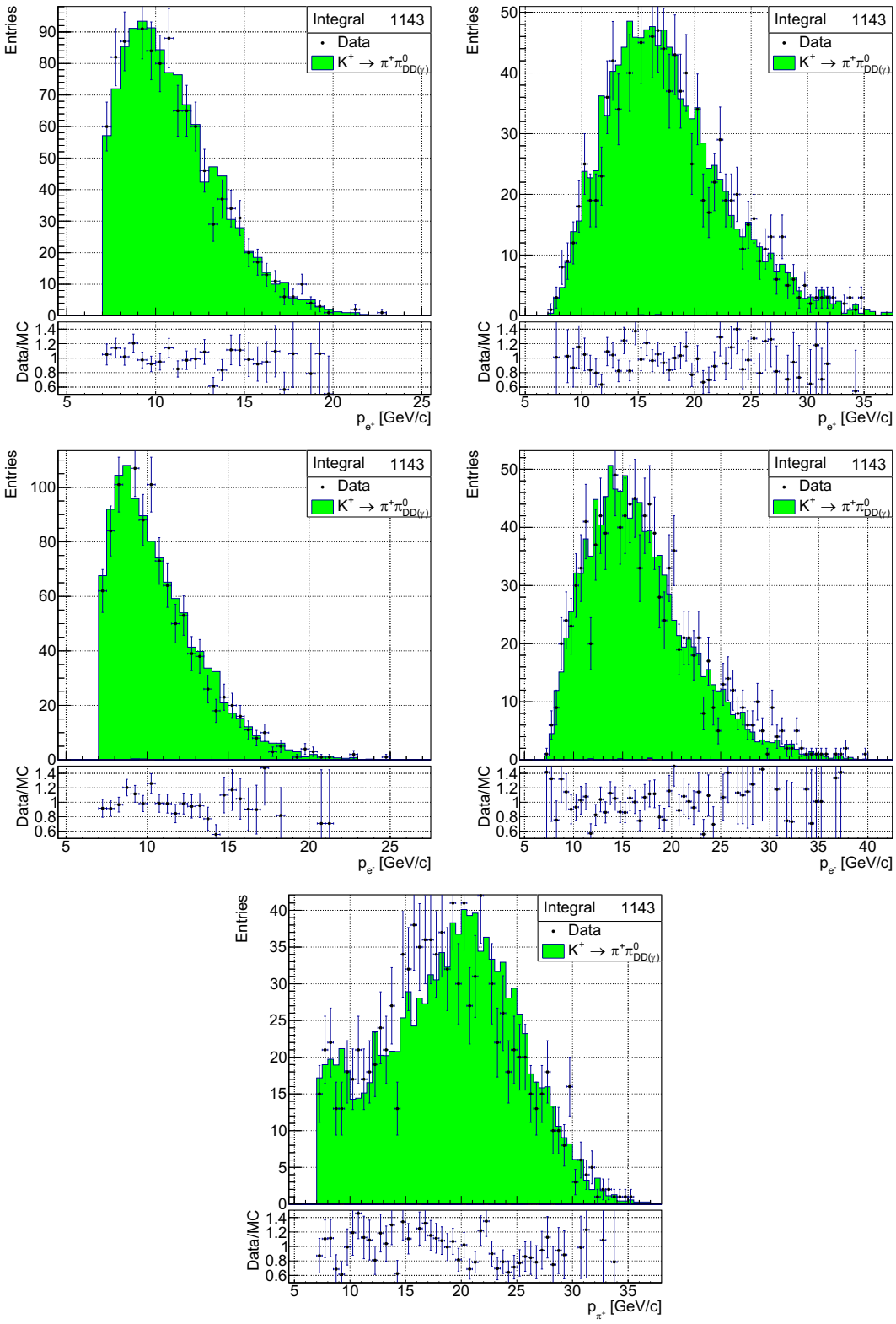

Figure 3.5: The momentum distributions of e^+ (top), e^- (middle), and π^+ (bottom). Since two positrons and two electrons occur in the final state, the momentum is shown for the lower-momentum (left) and the higher-momentum particle (right). Obtained from Run 1 data and the $K^+ \to \pi^+\pi^0_{DD(\gamma)}$ MC sample. The π^+ momentum distribution shows a significant discrepancy between data and MC.

3.3.3 Trigger Efficiency

The multi-track electron trigger is used in the present analysis. For the signal decay channel, measuring the trigger efficiency directly from the data is not possible since the statistics would not be sufficient in a control trigger sample. For MC events, the individual trigger conditions (table 2.4) are applied using emulated trigger response. The emulated trigger efficiency values for the corresponding trigger conditions are summarized in table 3.2.

Table 3.2: The emulated trigger efficiencies for individual eMT trigger conditions and for all conditions applied (full trigger application) in the signal selection. The first row provides the number of selected events before the trigger application (all the remaining cuts applied).

	N_{selected}	Efficiency [%]
No condition	8 857	
RICH	8 632	97.5
QX	8 506	96.0
E20	8410	95.0
KTAG	8 850	99.9
Straw-Exo	8 748	98.8
All conditions	8 098	91.4

3.4 Normalization Selection

Unlike the signal channel, the normalization channel $K^+ \to \pi^+ e^+ e^-$ has just three charged particles in the final state. The normalization selection uses a modified version of the analyzer from the NA62 framework [32] selecting the events with π^+, e^+, e^-, and it is described in the following text.

3.4.1 Three-track Vertex Selection

- The events containing three-track vertices with the charge +1, $\chi^2 < 30$, and z position 105 m $< z_{\text{vtx}} <$ 180 m are selected.
- The vertex momentum should not exceed the beam momentum by more than 5 GeV/c. The distance between the vertex and the beam axis should not exceed 40 mm.
- The difference between the vertex time (defined by the CHOD track times) and the trigger time is less than 5 ns. The KTAG candidate exists for the vertex with a time window of at most 2 ns.
- All tracks have to be consistent in time. For each two tracks, the CHOD time difference does not exceed 8 ns.
- As in the signal selection, photon conversions in the Straw material are suppressed by sufficient track separation at each Straw chamber. The minimal distance between each two tracks is required to be greater than 20 mm.

3.4.2 Particle Identification and Selected Samples

- The events containing exactly one good three-track vertex are considered.
- The basic $K^+ \to \pi^+\pi^+\pi^-$ decay rejection can be done in the following way: All 3 tracks are assumed to be pion tracks, the total invariant mass $m_{3\pi}$ distribution is constructed and the events with $m_{3\pi} < 500$ MeV/c^2 are rejected (fig. 3.6).

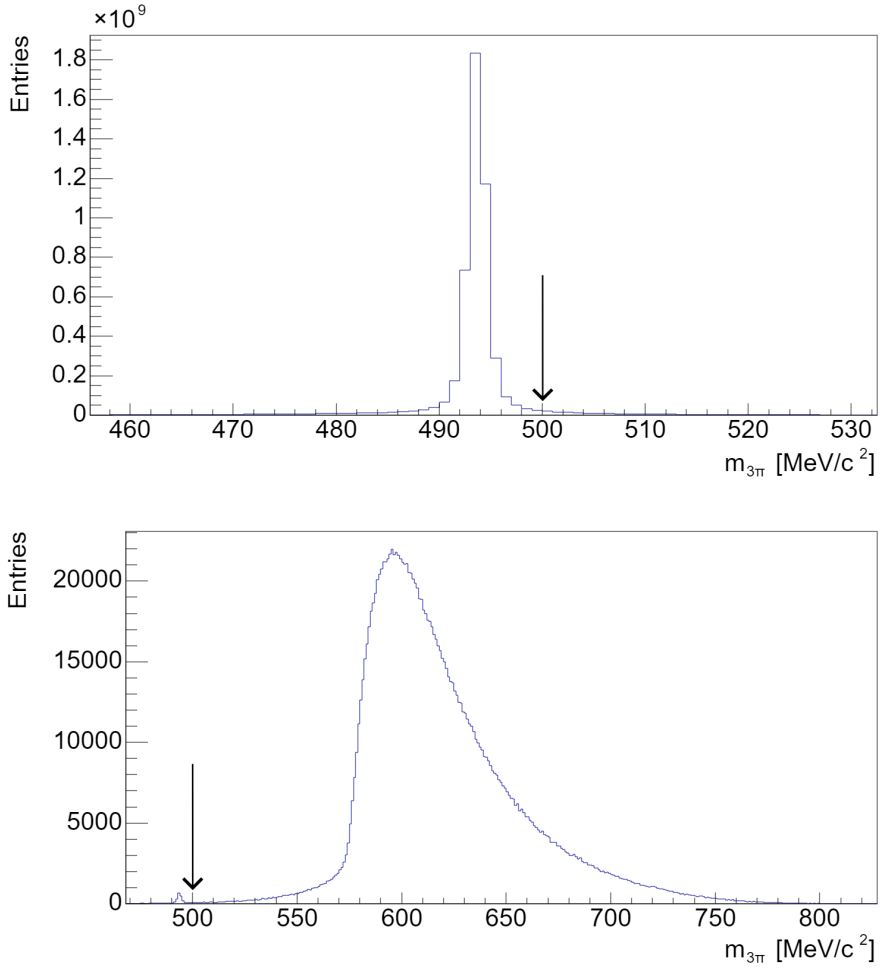

Figure 3.6: The $m_{3\pi}$ distribution assuming that all three tracks are pion tracks. Top: Run 1 data, bottom: $K^+ \to \pi^+e^+e^-$ MC simulation. The black vertical arrow indicates the lower cut on $m_{3\pi}$ invariant mass used in the selection.

- All the track momenta have to fulfill the condition 5 GeV/c < p_{track} < 65 GeV/c and the quality condition $\chi^2 < 20$. The difference between the momenta of the reconstructed tracks and the momenta before fit should not exceed 20 GeV/c.
- Each track is required to be in the acceptance of Straw, RICH, NA48-CHOD, CHOD, and LKr detector.
- Unlike the signal selection, the particle identification is based on the energy measurement in the LKr calorimeter (section 2.2.6). Namely, the ratio of

the track energy and momentum E/pc is measured, and the particles are identified in the following way:

→ e^-: the negative track with $0.9 < E/pc < 1.1$

→ e^+: the positive track with $0.9 < E/pc < 1.1$

→ π^+: the positive track with $E/pc < 0.85$

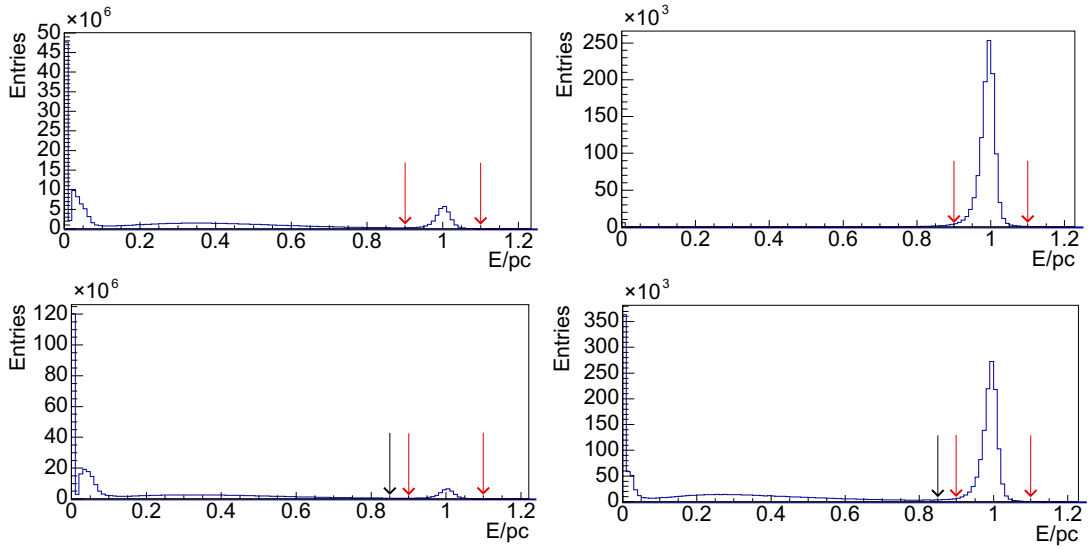

Figure 3.7: The E/pc distribution used for particle identification in the normalization selection. Top: negatively charged tracks, bottom: positively charged tracks, left: Run 1 data, right: $K^+ \to \pi^+e^+e^-$ MC sample. The black arrows indicate the maximal E/pc limit for a pion, and the red arrows correspond to the allowed range for electrons and positrons.

- The kinematic cuts on the electron-positron invariant mass m_{ee} and the total invariant mass $m_{\pi ee}$ are set as 140 MeV/c^2 $< m_{ee} <$ 360 MeV/c^2 and 480 MeV/c^2 $< m_{\pi ee} <$ 510 MeV/c^2.
- To suppress misidentified events, especially the $K^+ \to \pi^+\pi^0_D$ decays with $e^+ \leftrightarrow \pi^+$ misidentification which can lead to misreconstructed value of m_{ee} larger than 140 MeV/c^2, an additional kinematic cut is applied. The quantity m_{ee}(swap) is computed as the electron-positron invariant mass, but with the positron and the pion track identity swapped. The condition m_{ee}(swap) $>$ 110 MeV/c^2 is used.
- The vertex transverse momentum should not exceed 30 MeV/c, and the difference in momentum magnitudes between the vertex and beam should be less than 2500 MeV/c.
- As in the signal selection, the electron multitrack trigger (section 2.2.9), as well as the QX and E20 offline conditions, are applied. For MC, emulated individual trigger conditions forming the trigger line are applied.
- Event weights accounting for different three-track reconstruction efficiency in data and MC, measured in the NA62 internal note by Ľuboš Bičian [35], are applied to MC events.

The number of $K^+ \to \pi^+e^+e^-$ observed in Run 1 data is $N_{\text{norm}} = 12\,381$ and $M_{\text{norm}} = 454\,053$ in the $K^+ \to \pi^+e^+e^-$ MC sample. The number of generated events with the vertex z position in the interval (105, 180) m is $M_{\text{norm}}^{\text{ACC}} = 9\,745\,565$. The considered backgrounds are $K^+ \to \pi^+\pi^0_{DD(\gamma)}$ and $K^+ \to \pi^+\pi^0_D$; both are found to be negligible. The normalization and the resulting total number of decayed kaons N_K are:

$$\begin{aligned} A(K^+ \to \pi^+e^+e^-) &= (4.659 \pm 0.007) \times 10^{-2}, \\ N_K &= (8.86 \pm 0.36) \times 10^{11}. \end{aligned} \tag{3.10}$$

The distributions of invariant masses, particle momenta, and vertex z position are displayed in fig. 3.8 and fig. 3.9.

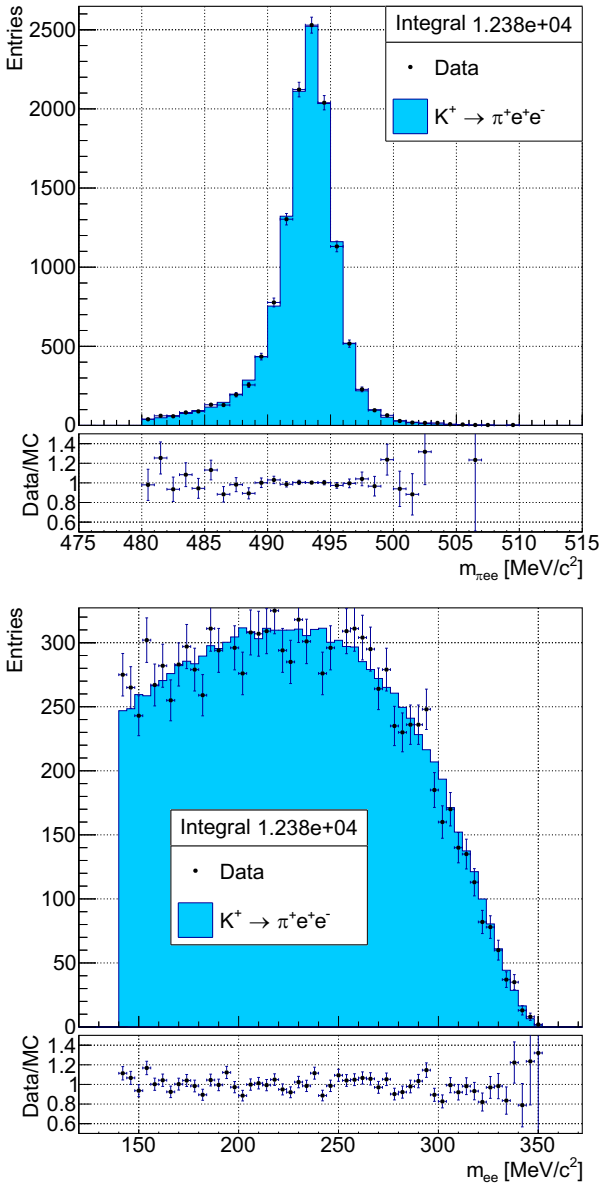

Figure 3.8: Top: $m_{\pi ee}$ invariant mass distribution, bottom: m_{ee} invariant mass distribution. The results are obtained from Run 1 data and $K^+ \to \pi^+e^+e^-$ MC sample.

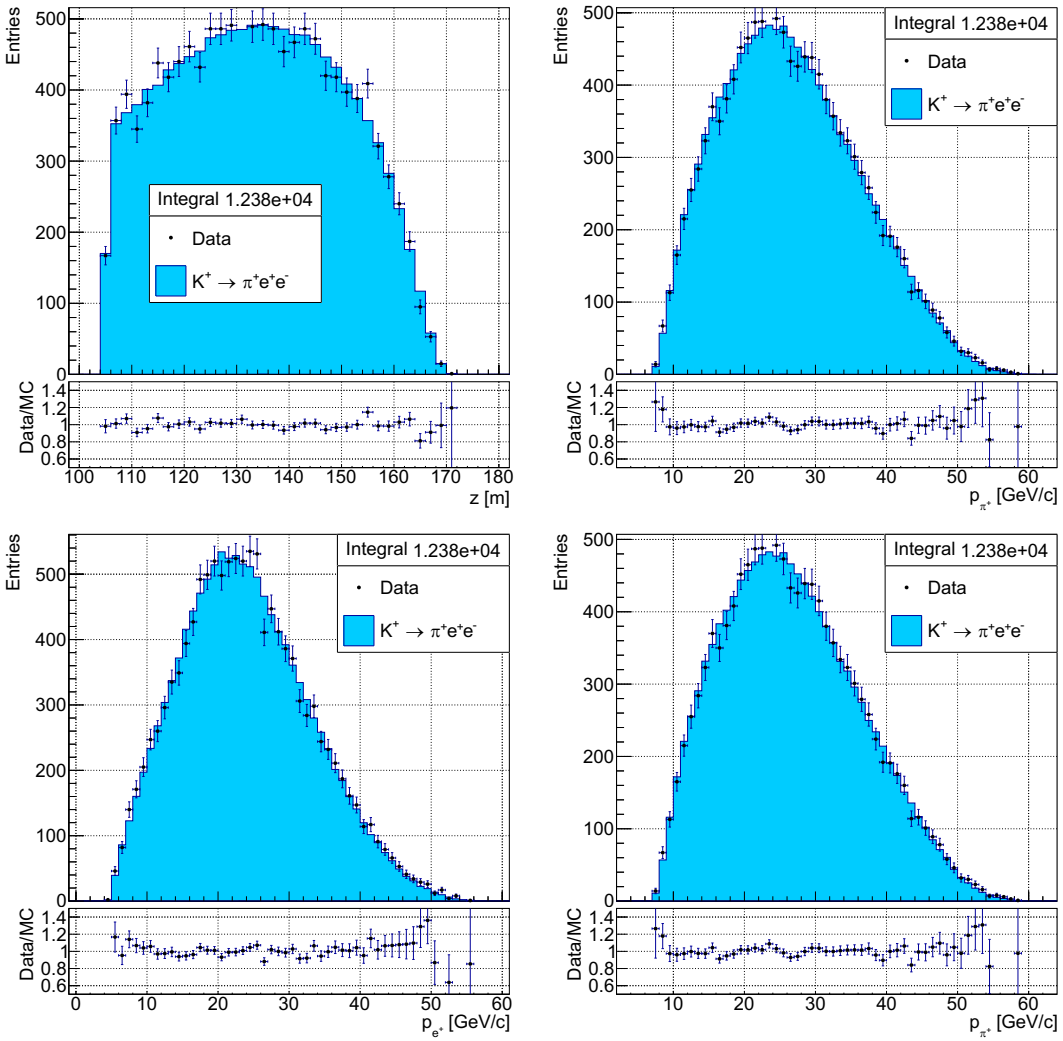

Figure 3.9: The vertex z position (top left) and the momentum of π^+ (top right), e^+ (bottom left), and e^- (bottom right).

3.4.3 Trigger Efficiency

The emulated trigger efficiencies for individual eMT trigger conditions were also evaluated for the normalization selection and are listed in table 3.3.

Table 3.3: The emulated trigger efficiencies for individual eMT trigger conditions and for all conditions applied (full trigger application) in the normalization selection. The first row provides the number of selected events before the trigger application (all the rest cuts applied).

	N_{selected}	Efficiency [%]
No condition	493 170	
RICH	481 923	97.7
QX	473 332	96.0
E20	478 651	97.1
KTAG	493 170	100.0
Straw-Exo	478 694	97.1
All conditions	454 053	92.1

3.5 Track Reconstruction Efficiency

After obtaining the signal and normalization samples and acceptances, it is important to investigate possible systematic effects present in the measurement. These effects can be present, for example, if the efficiency of a cut is different in the data with respect to the simulation, resulting in a wrong estimate of the acceptance. The present analysis identified the most important effect: the track reconstruction efficiency for five-track events. Other possible systematic effects include a data-MC mismatch in the trigger efficiency, spectrometer resolution, LKr response, etc., which will be studied in our future work, but are not included in this thesis. Given the experience from other analyses at NA62, their expected effect should be smaller than the one discussed in this section.

The quantity that we want to compare between data and simulation is the conditional probability of reconstructing all five tracks, given the particles crossed the active volume of the Straw spectrometer. One can use the MC truth information to make such an estimate for simulated events, but it is not possible to measure the quantity directly in data.

We developed a so-called probe method based on the search for the fifth reconstructed track, provided that four tracks from $K^+ \to \pi^+\pi^0_{DD}(\gamma)$ channel had already been reconstructed. A similar version of this method was previously developed for three-track reconstruction efficiency measurement used in the $K^+ \to \pi^+\mu^+\mu^-$ analysis by Ľuboš Bičian described in the NA62 internal note [35]. The procedure consists of the following steps:

1. A loop over all reconstructed four-track vertices is performed and the cuts analogous to the ones used for the signal selection are applied:
   - Vertex z-position is 105 m $< z_{\text{vtx}} <$ 180 m.
   - Vertex fit quality is $\chi^2 < 25$.
   - Vertex momentum satisfies $p_{\text{vtx}} < 70$ GeV/c.
   - The distance between a vertex and the beam does not exceed 40 mm.
   - Each track has fit quality $\chi^2 < 40$ and momentum 7 GeV/c $< p_{\text{track}} <$ 45 GeV/c.
   - The distance between a track and the beam does not exceed 50 mm.
   - Each track satisfies $|t_{\text{Straw}} - t_{\text{trigger}}| < 20$ ns.
   - Each track is required to be in the Straw geometric acceptance, and as for the signal selection, tracks have to be separated by at least 15 mm at each Straw chamber.
   - At least one KTAG candidate with at least 5 KTAG sectors and with $|t_{\text{vertex}} - t_{\text{KTAG}}|$ and $|t_{\text{trigger}} - t_{\text{KTAG}}| < 6$ ns must be present.
   - A GTK track with the maximal (and larger than 0.05) likelihood of being the correct match to the vertex is selected. The likelihood takes into account the distance between the vertex and the GTK candidate and the $t_{\text{KTAG}} - t_{\text{GTK}}$ time difference.
   - The electron multitrack trigger conditions (section 2.2.9) are applied.

- Particle identification of the four reconstructed tracks and of the remaining track not present in the four-track vertex (probe) is based on the decay kinematics. The PID procedure is described later in the text.

2. Probe charge is deduced from the total charge of the four-track vertex, assuming that the total charge is equal to one.

3. Probe momentum is computed using the GTK track momentum and the momenta of the tracks forming the corresponding four-track vertex.

4. The probe propagation downstream from the vertex through all Straw chambers is performed simulating a simple 270 MeV/c momentum kick in the x direction by the MNP33 magnet section 2.2.5. The probe is required to be in the Straw geometric acceptance.

5. The probe momentum has to be above 7 GeV/c, and the probe's radial distance from the center of the Straw chamber holes must be in the interval (100, 800) mm for each Straw chamber.

6. A reconstructed Straw track is matched to the probe if:

   - they have equal charge,
   - the difference of the momentum magnitudes does not exceed 5 GeV/c,
   - their maximum distance obeys the condition

   $$d_{\max} \; < \; (215 \; - \; \frac{p_{\text{track}}}{\text{GeV}/c} \; \cdot \; 2.5) \text{ mm}$$

   in all four Straw chambers. p_{track} stands for the momentum of the reconstructed Straw track.

Particle Identification in the Probe Efficiency Method

The four-track vertex can be composed of either 4 electron-like tracks (electron-like track means electron or positron) or 3 electron-like tracks and one pion track. The first option will be denoted as "missing pion" and the second "missing electron". The procedure of particle identification consists of the following steps:

1. The "missing pion" option is considered. Four-electron invariant mass is constructed as

   $$m^2_{eeee} = \left(\sum_{i=1}^{4} P_i \right)^2 , \tag{3.11}$$

   where P_i are the electron-like track four-momenta in the vertex. The missing invariant mass is computed as

   $$m^2_{\text{miss}(\pi)} = \left(P_K - \sum_{i=1}^{4} P_i \right)^2 . \tag{3.12}$$

   Then, a PID discriminant can be computed in the following way:

   $$D = \frac{\left(m^2_{\text{miss}(\pi)} - m^2_{\pi^+} \right)^2}{\sigma^2_{m^2_{\text{miss}(\pi)}}} + \frac{\left(m_{eeee} - m_{\pi^0} \right)^2}{\sigma^2_{m_{eeee}}}. \tag{3.13}$$

2. The option "missing electron" is considered. The vertex can contain 2 or 3 positively charged tracks. The loop over the positive tracks is performed, and each track is tested for the pion-identity hypothesis. From the momentum conservation law, the four-momentum of the missing electron-like particle $P_{\mathrm{miss}(e)}$ is computed. The missing mass squared is then $m^2_{\mathrm{miss}(e)} = P^2_{\mathrm{miss}(e)}$. The four-electron invariant mass is computed from the 3 reconstructed electron-like tracks plus the missing electron-like track:

$$m^2_{eeee} = \left(\sum_{i=1}^{3} P_i + P_{\mathrm{miss}(e)} \right)^2 . \tag{3.14}$$

The PID discriminant for each tested track is computed as

$$D = \frac{\left(m^2_{\mathrm{miss}(e)} - m^2_e \right)^2}{\sigma^2_{m^2_{\mathrm{miss}(e)}}} + \frac{\left(m_{eeee} - m_{\pi^0} \right)^2}{\sigma^2_{m_{eeee}}}. \tag{3.15}$$

3. The option with the lowest value of the discriminant D corresponds to the selected particle identification.

4. Kinematic cuts are applied for the selected PID combination.

   a) In the case of "missing pion":

$$\begin{aligned} |m_{eeee} - m_{\pi^0}| &< 10 \text{ MeV}/c^2, \\ |m_{\mathrm{miss}(\pi)} - m_{\pi^+}| &< 10 \text{ MeV}/c^2 \end{aligned} \tag{3.16}$$

   b) In the case of "missing electron":

$$\begin{aligned} |m_{eeee} - m_{\pi^0}| &< 10 \text{ MeV}/c^2, \\ |m^2_{\mathrm{miss}(e)} - m^2_e| &< 1000 \text{ MeV}^2/c^4. \end{aligned} \tag{3.17}$$

The corresponding 2D invariant mass distributions are shown in fig. 3.10.

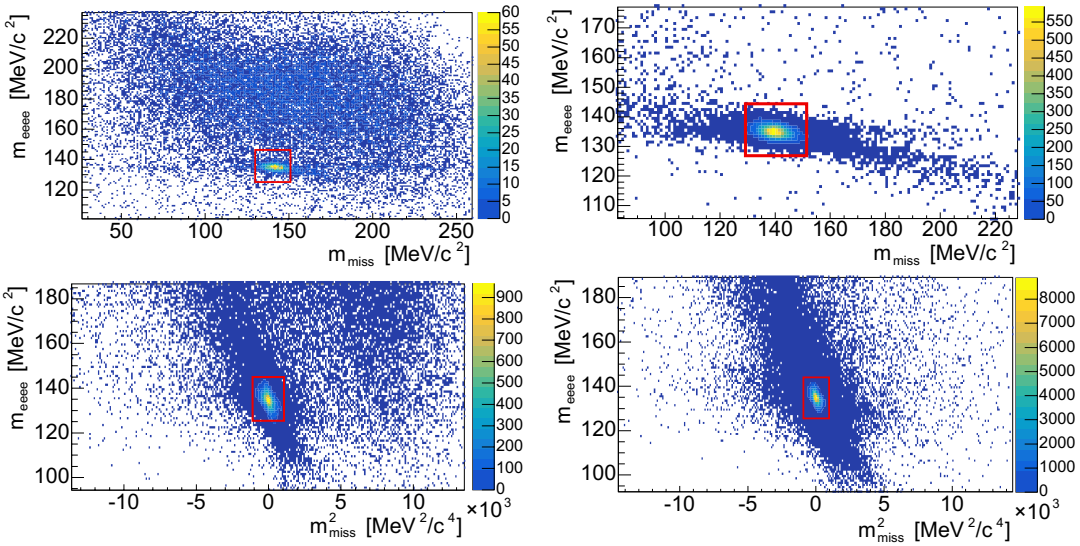

Figure 3.10: The 2D invariant mass distributions. Top: "missing pion" case, bottom: "missing electron" case, left: Run 1 data, right: signal MC sample. The red boxes indicate the invariant mass cuts.

Efficiency Results

There are two types of probe efficiency that one can evaluate using the events selected and identified by the described procedure:

a) Probe event efficiency: An event is considered efficient if at least one four-track vertex is selected, and its probe is matched to a reconstructed Straw track. If an event has at least one good four-track vertex with a good probe, but no Straw track was found to any of the good probes, such an event is inefficient. The probe event efficiency can be evaluated as a function of the missing particle (probe) identity and its momentum. A random good probe is selected for the identity/momentum classification if there are multiple good probes in an event.

b) Single-track efficiency: For each pair of a good vertex and a good probe (which could be either π^+, e^+, or e^-) one can evaluate a fraction of cases in which a reconstructed track matching to the probe was found. In this case, one event can be used to evaluate multiple single-track efficiencies. Single-track efficiency can be evaluated by looking among all reconstructed tracks or by looking only at tracks reconstructed using information from all 4 Straw chambers.

The overall probe event efficiency obtained from Run 1 data and the $K^+ \to \pi^+\pi^0_{DD(\gamma)}$ MC sample is listed in eq. (3.18) and the event efficiency as a function of probe momentum is shown in fig. 3.11. The efficiency is found to be significantly smaller in data than in MC, which has not been fully understood even after a detailed investigation. Similar three-track vertex probe efficiency as evaluated in [35] does not show such a disagreement. We also observe a significant drop in the event efficiency for pion probes in the momentum interval (10, 15) GeV/c, which will be a subject of future investigation in the π^0 double Dalitz analysis at NA62.

$$\begin{aligned} \epsilon_{\text{Data}}(\text{Probe}) &= (71.0 \pm 1.3)\% \\ \epsilon_{\text{MC}}(\text{Probe}) &= (75.9 \pm 1.5)\% \end{aligned} \tag{3.18}$$

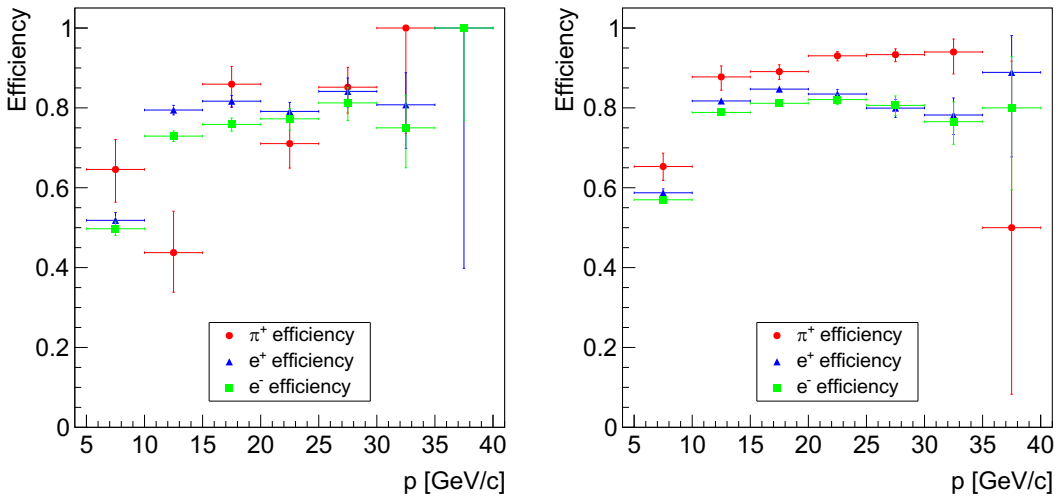

Figure 3.11: The probe event efficiency obtained from Run 1 data (left) and $K^+ \to \pi^+\pi^0_{DD(\gamma)}$ MC sample (right) as a function of the particle momentum.

The single-track reconstruction efficiency was also evaluated using the MC truth information, in which the probe position and momentum are exactly known. All the other particles are only required to be in the acceptance of all four Straw chambers in this MC-truth method. The efficiency can then be compared to the efficiency obtained using the probe single-track efficiency method. The overall results are listed in the following table. We observe reasonable agreement between the MC-truth and the probe method results obtained from MC. However, there is a significant disagreement between data and MC, especially for the pion track.

Table 3.4: The single-track reconstruction efficiency for π^+, e^+, and e^- obtained by MC truth method and probe method performed on the $K^+ \to \pi^+\pi^0_{DD(\gamma)}$ MC sample and Run 1 data.

	$\epsilon(\pi^+)$ [%]	$\epsilon(e^+)$ [%]	$\epsilon(e^-)$ [%]
MC-truth method	98.76 ± 0.02	88.87 ± 0.04	87.67 ± 0.04
Probe method – MC	$96.19^{+0.31}_{-0.33}$	$88.06^{+0.23}_{-0.24}$	$86.47^{+0.25}_{-0.26}$
Probe method – Data	$89.43^{+1.25}_{-1.39}$	$84.63^{+0.53}_{-0.54}$	$81.40^{+0.57}_{-0.59}$

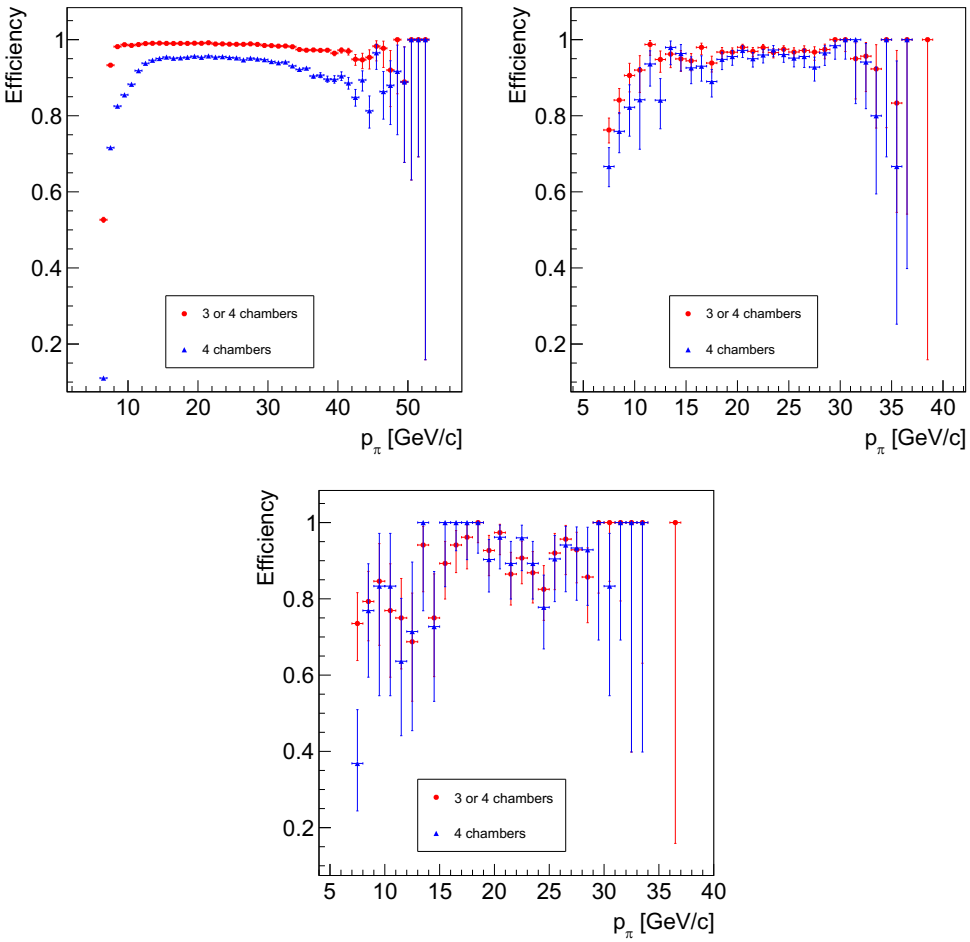

Figure 3.12: Pion single-track reconstruction efficiency. Top left: MC truth method, top right: probe method applied on the signal MC sample, bottom: probe method applied on the Run 1 data. Efficiency for the tracks reconstructed using the information from at least 3 Straw chambers (red) and exactly 4 chambers (blue).

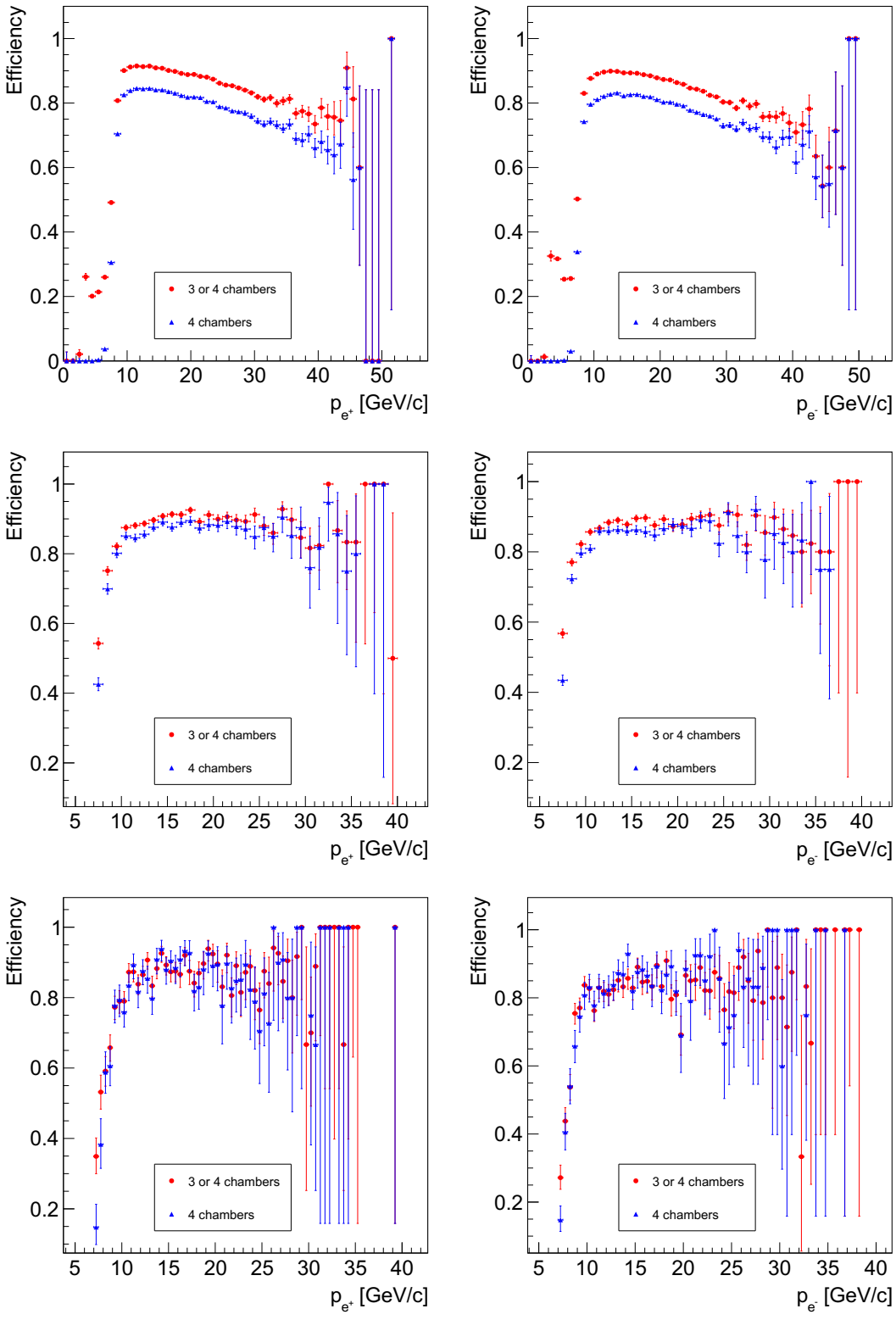

Figure 3.13: Single-track reconstruction efficiency of positron (left) and electron (right). Top: MC truth method, middle: probe method applied on the signal MC sample, bottom: probe method applied on the Run 1 data. Efficiency for the tracks reconstructed using the information from at least 3 Straw chambers (red) and exactly 4 chambers (blue).

Correction for the Branching Ratio Measurement

Given our observation that the track reconstruction efficiency for five-track events is significantly different between data and MC, we have to correct our simulated signal sample acceptance to take this fact into account for the branching ratio measurement. Even though the probe event efficiency depends on the probe momentum (fig. 3.11), we decided to include only the overall probe event efficiency values independent of the probe momentum in our result. The systematic correction factor C_{syst} is defined as

$$C_{\text{syst}} = \frac{\epsilon_{\text{Data}}(\text{Probe}) \times \epsilon_{\text{Data}}(\text{At least 4 tracks})}{\epsilon_{\text{MC}}(\text{Probe}) \times \epsilon_{\text{MC}}(\text{At least 4 tracks})}, \tag{3.19}$$

where $\epsilon_{\text{Data/MC}}(\text{Probe})$ are the overall probe event efficiencies obtained using the Run 1 data or the MC simulation which also includes minor background contributions from decays $K^+ \to \pi^+\pi^0_D$, $K^+ \to \pi^0_{DD}e^+\nu_e$, and $K^+ \to \pi^0_{DD}\mu^+\nu_\mu$ (eq. (3.18)). The quantities $\epsilon_{\text{Data}}(\text{At least 4 tracks})$ and $\epsilon_{\text{MC}}(\text{At least 4 tracks})$ are probabilities of reconstructing at least four out of five tracks in data and signal MC sample assuming that the full-event reconstruction efficiency factorizes into single-track efficiencies listed in table 3.4 (probe method). This assumption is not supported by evidence, but we have not identified a different method to correct for the efficiency of four-track vertex reconstruction. The values under the listed assumption are:

$$\begin{aligned} \epsilon_{\text{Data}}(\text{At least 4 tracks}) &= (82.3 \pm 1.3)\%, \\ \epsilon_{\text{MC}}(\text{At least 4 tracks}) &= (90.5 \pm 0.4)\%. \end{aligned} \tag{3.20}$$

The correction factor is then used to modify the signal acceptance

$$A(K^+ \to \pi^+\pi^0_{DD(\gamma)}) \to A(K^+ \to \pi^+\pi^0_{DD(\gamma)}) \times C_{\text{syst}} \tag{3.21}$$

The correction factor and the modified signal acceptance are:

$$\begin{aligned} C_{\text{syst}} &= 0.850 \pm 0.027, \\ A(K^+ \to \pi^+\pi^0_{DD(\gamma)}) &= (2.004 \pm 0.022_{\text{stat}} \pm 0.064_{\text{syst}}) \times 10^{-4}. \end{aligned} \tag{3.22}$$

The quoted systematic uncertainty in the modified acceptance originates from the error in the C_{syst}, which is of statistical origin (limited data and MC sample sizes used to evaluate efficiencies). A proper estimate of the systematic uncertainty requires further studies of the reconstruction efficiency mismatch between data and MC.

3.6 Branching Ratio Measurement Result

This section summarizes the results discussed in section 3.3, section 3.4 and provides our measured value of the π^0 double Dalitz decay branching ratio. In Run 1 data we observed 1143 $K^+ \to \pi^+\pi^0_{DD(\gamma)}$ events and 12 381 $K^+ \to \pi^+e^+e^-$ events. The signal and normalization acceptances which include the systematic correction for the track reconstruction efficiency, are:

$$\begin{aligned} A(K^+ \to \pi^+\pi^0_{DD(\gamma)}) &= (2.004 \pm 0.067) \times 10^{-4}, \\ A(K^+ \to \pi^+e^+e^-) &= (4.659 \pm 0.007) \times 10^{-2}. \end{aligned} \tag{3.23}$$

The backgrounds to the signal and normalization channels can be neglected as discussed in section 3.3 and section 3.4. Using the results listed above and the formula

$$B(\pi^0_{DD(\gamma)}) = \frac{N_{\text{sig}}}{N_{\text{norm}}} \frac{A(K^+ \to \pi^+e^+e^-)B(K^+ \to \pi^+e^+e^-)}{A(K^+ \to \pi^+\pi^0_{DD(\gamma)})B(K^+ \to \pi^+\pi^0)},$$

the π^0 double Dalitz decay branching ratio is

$$\begin{aligned} B(\pi^0_{DD(\gamma)}, x_{4e} > 0.9) &= (3.12 \pm 0.10_{\text{stat}} \pm 0.10_{\text{syst}} \pm 0.09_{\text{ext}}) \times 10^{-5} \\ &= (3.12 \pm 0.17) \times 10^{-5}. \end{aligned} \tag{3.24}$$

The uncertainty is split into a statistical component involving the uncertainties originating from the number of selected events in Run 1 data and the MC acceptances, a systematic component involving the uncertainty of C_{sys} (section 3.5), and an external component originating from the uncertainties of used branching ratios [5]

$$\begin{aligned} B(K^+ \to \pi^+e^+e^-) &= (3.00 \pm 0.09) \times 10^{-7}, \\ B(K^+ \to \pi^+\pi^0) &= (20.67 \pm 0.08)\%. \end{aligned}$$

The result is compatible with the KTeV measurement $B^{x>0.9}_{eeee} = (3.26 \pm 0.18) \times 10^{-5}$ (section 1.4, eq. (1.8)) with a similar total uncertainty. However, it should be noted that our study of systematics is not complete, and the mismatch in the track reconstruction needs to be investigated further.

Conclusion

In this master's thesis, we have presented the π^0 double Dalitz decay branching ratio measurement using the NA62 experiment data sample collected in 2017 and 2018 (Run 1 data). The measured branching ratio is inclusive of final-state photon radiation, with the kinematic region defined as $x_{4e} = (m_{eeee}/m_{\pi^0})^2 > 0.9$. The number of selected $K^+ \to \pi^+\pi^0_{DD(\gamma)}$ events in the Run 1 data is 1143. The result of our analysis is

$$\begin{aligned} B(\pi^0_{DD(\gamma)}, x_{4e} > 0.9) &= (3.12 \pm 0.10_{\text{stat}} \pm 0.10_{\text{syst}} \pm 0.09_{\text{ext}}) \times 10^{-5} \\ &= (3.12 \pm 0.17) \times 10^{-5}. \end{aligned}$$

The measurement's relative uncertainty is 5.5%. Five-track reconstruction efficiency was identified as the main systematic uncertainty in the analysis. A probe-based method was developed to measure track reconstruction efficiency, and the values measured in the data and simulated samples were used to evaluate a correction for the simulation. The measured reconstruction efficiencies in Run 1 data are approximately 5% lower than in simulated $K^+ \to \pi^+\pi^0_{DD(\gamma)}$ events. This discrepancy needs to be studied in future analysis of the π^0 double Dalitz decay at NA62.

The NA62 experiment has been collecting new data since 2021 (Run 2). By the end of the NA62 data taking (CERN Long Shutdown 3), the di-electron dataset size is estimated to increase by a factor of 10, which should significantly improve the measurement precision.

Bibliography

[1] Steven Weinberg. A Model of Leptons. *Phys. Rev. Lett.*, 19:1264–1266, Nov 1967.

[2] Sheldon L. Glashow. Partial-symmetries of weak interactions. *Nuclear Physics*, 22(4):579–588, 1961.

[3] Abdus Salam. Weak and Electromagnetic Interactions. *Conf. Proc. C*, 680519:367–377, 1968.

[4] G. 't Hooft and M. Veltman. Regularization and renormalization of gauge fields. *Nuclear Physics B*, 44(1):189–213, 1972.

[5] P.A. Zyla et al. Review of Particle Physics. *PTEP*, 2020(8):083C01, 2020. and 2021 update.

[6] R. G. Sachs. CP Violation in K^0 decays. *Phys. Rev. Lett.*, 13:286–288, Aug 1964.

[7] A. Alavi-Harati et al. Observation of direct CP violation in $K_{S,L} \to \pi\pi$ decays. *Phys. Rev. Lett.*, 83:22–27, 1999.

[8] V. Fanti et al. The Beam and detector for the NA48 neutral kaon CP violations experiment at CERN. *Nucl. Instrum. Meth. A*, 574:433–471, 2007.

[9] Eduardo Cortina Gil et al. The Beam and detector of the NA62 experiment at CERN. *JINST*, 12(05):P05025, 2017.

[10] C. C. Butler G. D. Rochester. Evidence for the Existence of New Unstable Elementary Particles. *Nature*, 1947.

[11] P. H. Fowler R. BrownMiss, U. Camerini. Observations with Electron-Sensitive Plates Exposed to Cosmic Radiation. *Nature*, 1949.

[12] A. Pais. Some Remarks on the v-Particles. *Phys. Rev.*, 86:663–672, Jun 1952.

[13] M. Gell-Mann. Isotopic Spin and New Unstable Particles. *Phys. Rev.*, 92:833–834, Nov 1953.

[14] Michal Koval'. *Measurement of Neutral Pion Transition Form Factor and Contributions to Trigger and Data Acquisition System at NA62 Experiment at CERN.* PhD thesis, Comenius University in Bratislava Faculty of Mathematics, Physics and Informatics, 2016.

[15] Buras Andrzej J., Buttazzo Dario, Girrbach-Noe Jenifer. *et al.* $K^+ \to \pi^+\nu\bar{\nu}$ and $K_L \to \pi^0\nu\bar{\nu}$ in the Standard Model: status and perspectives. *Journal of High Energy Physics*, (33), 2015.

[16] Andrzej J. Buras. Weak Hamiltonian, CP Violation and Rare Decays, 1998.

[17] Artamonov A. et al. Study of the decay $K^+ \to \pi^+\nu\overline{\nu}$ in the momentum region $140 < P_\pi < 199\text{MeV}/c$. 79:092004, May 2009.

[18] Eduardo Cortina Gil et al. Measurement of the very rare $K^+ \to \pi^+\nu\overline{\nu}$ decay. *JHEP*, 06:093, 2021.

[19] Hideki YUKAWA. On the Interaction of Elementary Particles. I. *Proceedings of the Physico-Mathematical Society of Japan. 3rd Series*, 17:48–57, 1935.

[20] Shoichi Sakata and Yasutaka Tanikawa. The Spontaneous Disintegration of the Neutral Mesotron (Neutretto). *Phys. Rev.*, 57:548–548, Mar 1940.

[21] G. P. S. Occhialini and C. F. Powell. Nuclear disintegration produced by slow charged particles of small mass. *Nature*, 159:186–190, 1947.

[22] R. Bjorklund, W. E. Crandall, B. J. Moyer, and H. F. York. High Energy Photons from Proton-Nucleon Collisions. *Phys. Rev.*, 77:213–218, Jan 1950.

[23] L.G. Landsberg. Electromagnetic decays of light mesons. *Physics Reports*, 128(6):301–376, 1985.

[24] Murray Gell-Mann and Fredrik Zachariasen. Form Factors and Vector Mesons. *Phys. Rev.*, 124:953–964, Nov 1961.

[25] A. R. Barker, H. Huang, P. A. Toale, and J. Engle. Radiative corrections to double Dalitz decays: Effects on invariant mass distributions and angular correlations. *Phys. Rev. D*, 67:033008, Feb 2003.

[26] Tomáš Husek. Update on π^0 decays (NA62 internal presentation), Precision WG meeting, 23.5.2024.

[27] KTeV Collaboration. Determination of the Parity of the Neutral Pion via Its Four-Electron Decay. *Phys. Rev. Lett.*, 100:182001, May 2008.

[28] The NA62 collaboration. Development of a new CEDAR for kaon identification at the NA62 experiment at CERN. *Journal of Instrumentation*, 19(05):P05005, May 2024.

[29] F Hahn, F Ambrosino, A Ceccucci, H Danielsson, N Doble, F Fantechi, A Kluge, C Lazzeroni, M Lenti, G Ruggiero, M Sozzi, P Valente, and R Wanke. NA62: Technical Design Document. Technical report, CERN, Geneva, 2010.

[30] NA48 Collaboration. The beam and detector for the NA48 neutral kaon CP violation experiment at CERN. *Nuclear Instruments and Methods in Physics Research Section A: Accelerators, Spectrometers, Detectors and Associated Equipment*, 574(3):433–471, 2007.

[31] The NA62 Collaboration. Performance of the NA62 trigger system, 2023.

[32] NA62 Collaboration. NA62 Framework. https://na62-sw.web.cern.ch/.

[33] J. Allison et al. Recent developments in Geant4. *Nucl. Instrum. Meth. A*, 835:186–225, 2016.

[34] Eduardo Cortina Gil et al. Search for K^+ decays into the $\pi^+e^+e^-e^+e^-$ final state. *Phys. Lett. B*, 846:138193, 2023.

[35] Ľuboš Bičian. New Measurement of $K^+ \to \pi^+\mu^+\mu^-(\gamma)$ Decay with NA62 Run 1 Data (NA62 internal note), 2022.